Brightness Measurements of Stars and the Night-Sky with a Silicon-Photomultiplier-Telescope

von

Rebecca Meißner

Bachelorarbeit in Physik

vorgelegt der
Fakultät für Mathematik, Informatik und Naturwissenschaften
der
Rheinisch-Westfälischen Technischen Hochschule Aachen

Vorgelegt im September 2012

angefertigt am

III. Physikalischen Institut A

Gutachter und Betreuer

Prof. Dr. Thomas Hebbeker
III. Physikalisches Institut A
RWTH Aachen

Contents

List of Figures

1. Introduction

The night-sky has always caught mankind's interest and provoked on people to obtain a deeper understanding of the universe. Since recently, methods to investigate information contained in particles coming to Earth are developed.

Astroparticle physics is a relatively new area of research combining high energy particle physics, astrophysics and cosmology within which ultra-high-energy cosmic rays (UHECRs) are an issue of current basic research. The cosmic ray particles constantly hit the atmosphere and initiate a cascade of secondary particles. Altogether, they form an extensive air shower. Several particles, especially positrons and electrons, excite the Nitrogen molecules of the air. As result of their de-excitation, weak ultraviolet light is radiated.

This fluorescence light can be detected with fluorescence detectors. Since the signal is very weak efficient detectors are needed. Currently, photomultiplier tubes (PMTs) are used in experiments such as the Pierre Auger Observatory in Argentina.

A new promising technology of fluorescence light detection are silicon photomultipliers (SiPMs). SiPMs are semiconductors enabling measurements with even higher efficiency in single photon counting mode than photomultiplier tubes. A new telescope aiming at demonstrating that the detection of fluorescence light is possible with SiPMs is FAMOUS. The acronym stands for First Auger Multi-Pixel-Photon-Counter camera for the Observation of UHECR air Showers.

The origin of detected photons are both the fluorescence light evoked by UHECRs and all other light sources summarised as night-sky brightness. As FAMOUS is liked to be tested in Aachen some questions raise, e.g.: Is it dark enough in Aachen to measure UHECRs? What is the background luminosity in Aachen? Summing up the main idea of these question in one question: How many photons will FAMOUS detect? Within the simulation of FAMOUS it is essential categorising the light flux caused by the night-sky brightness to distinguish between air showers (or rather cosmic ray events) and background. Based on this information a threshold value and trigger are implemented and measurements are started when showers arrive.

In the context of this thesis measurements of stars and the night-sky brightness have been performed with a one-pixel-silicon-photomultiplier telescope. This thesis is to present and evaluate the taken data. After a theoretical introduction into UHECRs, the night-sky brightness and SiPMs, the analysis algorithm is explained. Furthermore, all undesired effects contributing to the change of the calculated light flux are discussed and determined. Finally, measurement results are presented.

2. Cosmic Rays and Night-Sky Brightness

One objective in current fundamental research is the detection of ultra-high-energy cosmic rays (UHECRs) and its information readout. In this context one has to distinguish between signal (the UHECRs) and the background which in this case is the night-sky brightness (NSB). After determining the background effects, the value can be implemented in simulation, in this case the simulation for the FAMOUS telescope. Constantly the signal-to-noise-ratio is calculated and if a certain level is exceeded a measurement is triggered for the detection of UHECRs.

2.1 Cosmic Rays

Ultra-high-energy cosmic rays are particles from the cosmos with energies up to several 10^{20} eV. Their sources are still unknown and hence a topic of research. The energy spectrum of cosmic rays follows a steep power law continuously falling with the amount of energy of one particle. Consequently, particles with very high energies are rarely hitting the atmosphere, e.g. the flux at energies of about 10^{20} eV is one particle per century and km^2 [1].

Extensive Air Showers

On account of the very low flux the study of UHECRs requires large, ground based detection areas. During their path through the atmosphere of the Earth, the highly energetic particles interact with molecules and, as a result, arise secondary particles. These again interact with the atmosphere or decay. One or more particle cascades are initiated, also referred to as extensive air shower. Therefore, only the detection of the multiple secondary particles is reasonable but not of the UHECRs themselves [1].

Besides the creation of new particles, Nitrogen molecules in the atmosphere are excited especially by the electrons and positrons of the secondary particles. With the de-excitation of the Nitrogen, fluorescence light in the ultraviolet up to the visible-blue range is emitted [1].

The fluorescence light spectrum is shown in figure 2.1.

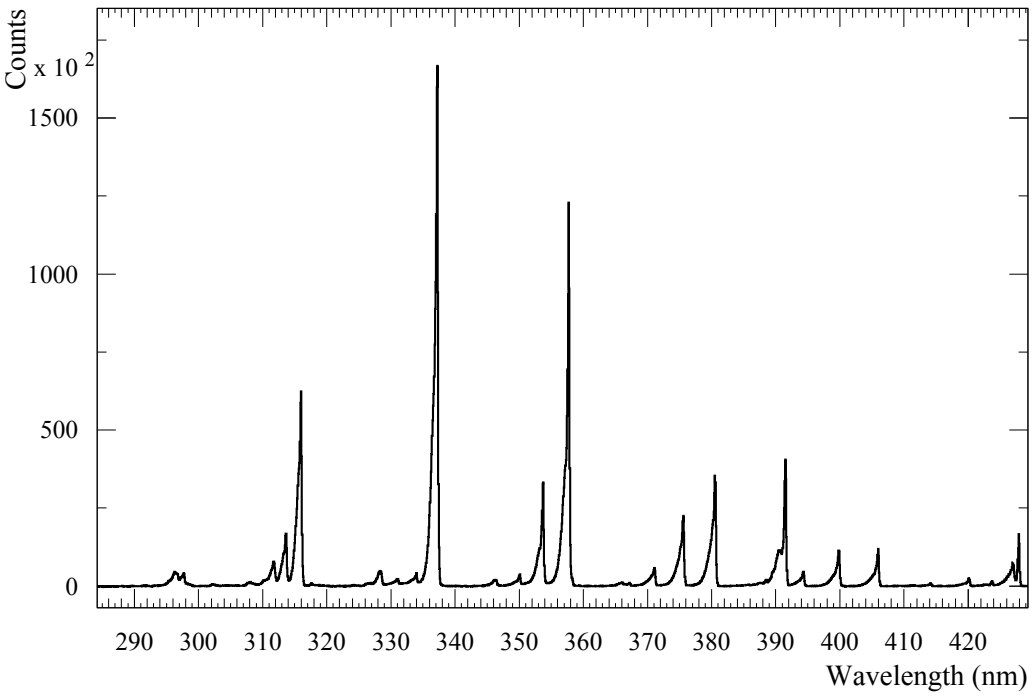

Figure 2.1: Fluorescence light spectrum measured by the AIRFLY experiment. The spectrum in dependency of the wavelength λ has been performed in dry air with a 3 MeV electron beam at 800 hPa and 293 K [1].

.

2.1.1 Pierre Auger Observatory

The Pierre Auger Observatory is currently the largest experiment detecting ultra-high-energy cosmic rays. It is located in the Argentinian Pampa Amarilla since this region near Malargüe obtains very good conditions, e.g. a pure atmosphere with clean air and few light pollution, geographical situation, height above sea level and a flat surface [2].

The observatory compounds a surface detector (SD) and a fluorescence detector (FD) to a hybrid detector. The surface detector consists of 1600 hexagonal arranged water Cherenkov stations. Each SD station comprises 12 tons ultra-pure water and 3 photomultiplier tubes (PMTs) for the detection of Cherenkov light emitted by secondary particles in the water. The area covered with these tanks measures about 3000 km^2 with a distance of 1.5 km between the stations [4].

The fluorescence detector overlooks this area. For this purpose, there are 4 buildings housing 6 telescopes each[1] (cf. fig. 2.2). The focal surface of a fluorescence telescope is built up of an array of 440 PMTs having a total field of view of 30° x 30°. In the wavelength range $(350 - 400)$ nm the PMTs currently used at the Pierre Auger Observatory reach a maximal quantum efficiency of 30 % [6]. To reduce the noise due to visible light entering the telescope an ultraviolet and partially infrared light

[1]Not included is the HEAT extension consisting of 3 telescopes, for further information refer to [5]

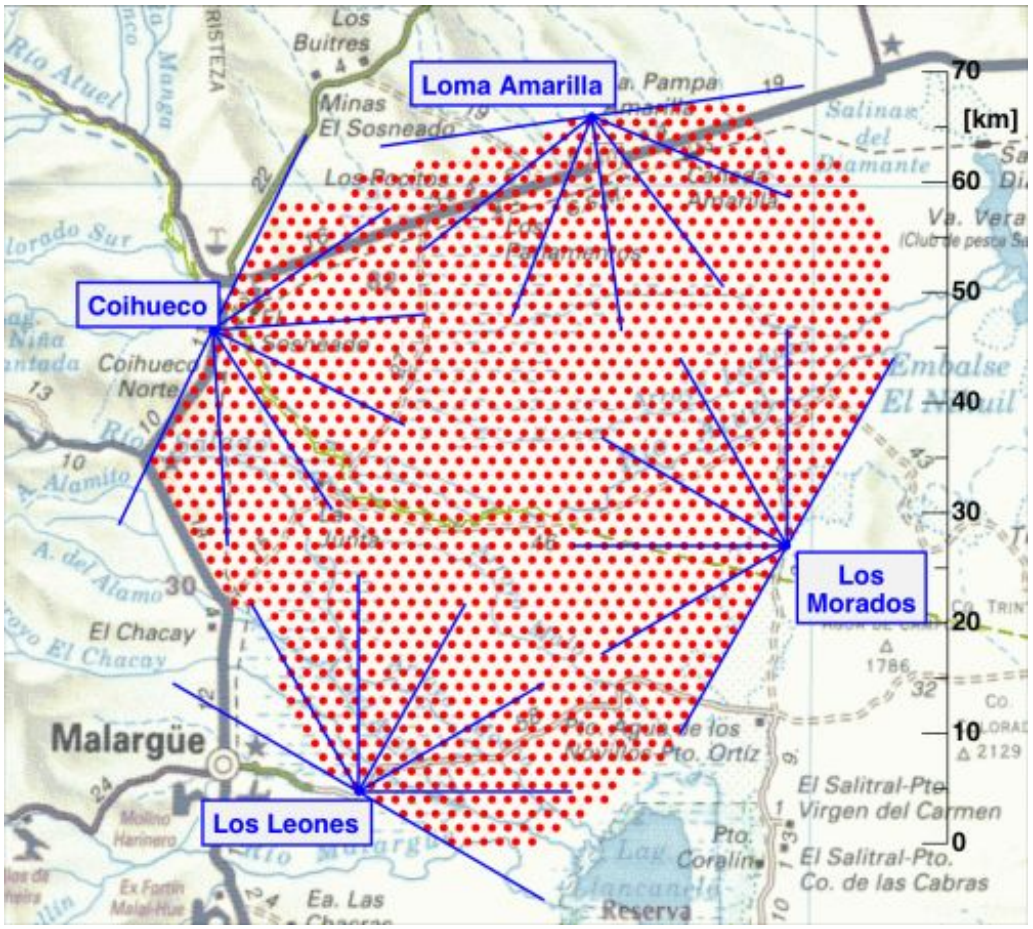

Figure 2.2: Map of the southern site of the Pierre Auger Observatory. The surface detectors are indicated by the red dots. The fluorescence detector visualised in blue overlooks the area and consists of four telescope buildings. The blue lines mark their field of view [3].

transparent filter is used (the transmission as a function of the wavelength is plotted in fig. 6.3).

Whereas the surface detector has a duty cycle of nearly 100 % the fluorescence detector operates only in starlit and moonless nights and therefore has a duty cycle of $(10 - 15)$ % [6].

FAMOUS

The FAMOUS prototype telescope aims to demonstrate that light detection with silicon photomultiplier telescopes is possible and more efficient than with PMTs [7]. SiPMs are expected to reach higher photon detection efficiencies than PMTs and therefore enable more sensitive measurements of showers less intense in light. In this context, a prototype with 64 pixels and a total field of view of 12° was designed and simulations have been performed showing FAMOUS being able to detect air showers [8]. For the simulations of FAMOUS background values are needed. Hence, night-sky brightness measurements without ultraviolet-pass filter were performed

revealing it to be the dominant background source [9]. To implement even more exact values in upcoming simulations new data was taken being the basis of this work.

2.2 Night-Sky Brightness

The night-sky brightness is composed of two main fields: Natural light and light caused by civilisation commonly named light pollution. In astronomical publications the brightness is given in units of mag $\cdot$ arcsec^{-2}. Magnitude (mag) is a unit for the luminous intensity which depends logarithmically on the SI-unit Candela [10]:

$$m_1 - m_2 = -2.5 \cdot \log_{10}\left(\frac{s_1}{s_2}\right) \tag{2.1}$$

with s_1 and s_2 the luminous flux (per solid angle) of two different objects and m_1 and m_2 their values of magnitude (per arcsec^2). The logarithmic scale enables astronomers to classify less light-intense celestial bodies into finer sections. With increasing brightness the magnitude gets smaller. The division by arc-second squared (arcsec^{-2}) includes the solid angle dependency. Frequently, the brightness is also given in units of S_{10}. The brightness of an object of one S_{10} is equal to the brightness of one star of magnitude 10 per square degree (which equals 27.78 mag arcsec^{-2}).

The S_{10} system is commonly applied for extended objects and within comparisons between the brightness of objects as it is a linear system. Magnitude (per arcsec^2) (m_g) can be converted into the number of tenth magnitude stars (per arcsec^2) (I_g) by equation (2.2) [11]:

$$I_\mathrm{g} = 10^{(-0.4\,(m_\mathrm{g}-10))} \quad . \tag{2.2}$$

To enable the subdivision of the apparent brightness of objects into size categories a zero point is needed. Vega was chosen to be this reference star and its magnitude was set to 0 mag [10].

For measurements filters are used to subdivide the brightness into wavelength bands i.a. red (R-band), visible (V-band) and blue (B-band). In astronomical publications the brightness in the different bands are given in units of mag arcsec^{-2} if not otherwise stated. This notation is taken in this thesis as well.

The natural light is compounded of several effects and sources itself. Variation within the natural light are mainly caused by moonlight. During moonless nights at high elevation, high galactic latitude and high ecliptic latitude the median night-sky brightness (also called zenith brightness) measures about B = 22.7, V = 21.9 (corresponding to 220 S_{10}) and R = 21.0 (with similar values at other dark sites) [12].

The main contributions to natural light are airglow and zodiacal light followed by starlight, diffuse galactic and extragalactic light (cf. tab. 2.1). As not otherwise

Component	**V_{zenith} / S_{10} units**
Airglow	145
Zodiacal light	60
Starlight	
$V > 20$, integrated light	< 55
scattered light by interstellar dust	10
Extragalactic light	~ 1
Total	**220**

Table 2.1: Natural light split into its components. The brightness indicated is the zenith brightness for the V-band V_{zenith} in units of S_{10}. Taken from [12].

marked information from this section are found in [12] (a summary of this publication is presented in [13]).

Airglow is used to describe the emission of photons by atoms or molecules in the upper atmosphere. These are excited by solar UV radiation during daytime and emit photons while de-exciting. Airglow contributes with $V = 145\ S_{10}$ to the night-sky brightness. It is negligible at latitudes smaller than 40° (or rather bigger than 320°).

Zodiacal light is mainly observed after the sunset or before the sunrise. It is caused by sunlight scattered by interplanetary dust. The brightness amounts to $V = 60\ S_{10}$.

Starlight has to be distinguished into light of bright and visible stars (with brightnesses in the V band of about 20 mag $\cdot$ arcsec^{-2}) and the light of the regions in between. In this regions a diffuse glow is measurable due to starlight scattering on interstellar dust. First contributes with less than $V = 55\ S_{10}$, the last with $V = 10\ S_{10}$.

Extragalactic light, i.a. light of star formation, is the weakest component with around $V = 1\ S_{10}$.

The moonlight has a strongly varying effect on the night-sky brightness. It is a function depending on the phase of the Moon, the zenith distance of the Moon, the zenith distance of the sky position, the angle between the Moon and the sky position and the atmospheric extinction [14]. The approximate maximal contribution is around 4 mag arcsec^{-2} during full moon and a separation of moon and field of view greater than 10°. An accurate model of the dependencies can be found in [14].

In contrast to the natural light, light pollution differs strongly depending on the site of observation. Close to civilization light pollution may dominate the night-sky brightness. Many effects count into this area such as street lighting, cars, satellites, aeroplanes and lighting in houses. To specify the amount contributing to the night-sky brightness (NSB) measurements in regions with low and high population density can be compared to get estimated values. This method has been pursued in this thesis.

3. Light Detection with Silicon Photomultipliers

A relatively young and promising technology for the detection of low light levels or even single photons are silicon photomultipliers (SiPMs). The following chapter explains their functioning, noise effects they have and how SiPM signals are processed.

3.1 Silicon Photomultipliers

SiPMs are arrays of Geiger-mode avalanche photodiodes (G-APDs). The photodiodes are junctions of p- and n-doped semiconductors with the p-doped layers being connected to the anode and the n-doped layers to the cathode (cf. fig. 3.1). At the p-n-junctions a zone of depletion is formed and broadened when applying a reverse bias voltage V_{bias}.

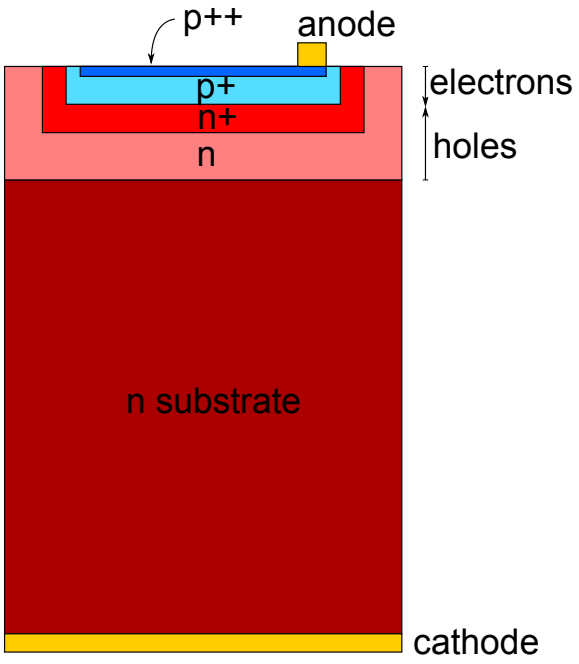

Figure 3.1: Schematic of an avalanche photodiode. p- and n-doped layers are themselves divided into sections of different doping. Adapted from [15].

A photon reaching the depletion zone might be absorbed and create an electron-hole pair. The high electric field accelerates the charge carriers. If the energy gain of

both electron and hole is high enough for impact ionisation the photodiode operates in Geiger-mode. The minimal voltage at which this occurs is the breakdown voltage V_{BD}. The voltage difference between bias-voltage and breakdown-voltage is refered to as over-voltage V_{OV}

$$V_{OV} = V_{bias} - V_{BD} > 0 \quad . \tag{3.1}$$

The initiated avalanche is self-sustaining. Therefore, a quenching resistor connected in series is necessary to stop the process: The increase of photocurrent during the avalanche causes an increasing voltage at the quenching resistor and consequently a decreasing voltage at the diode. As a result, the avalanche is stopped and the photodiode reverts to its initial state. The time needed is refered to as recovery time.

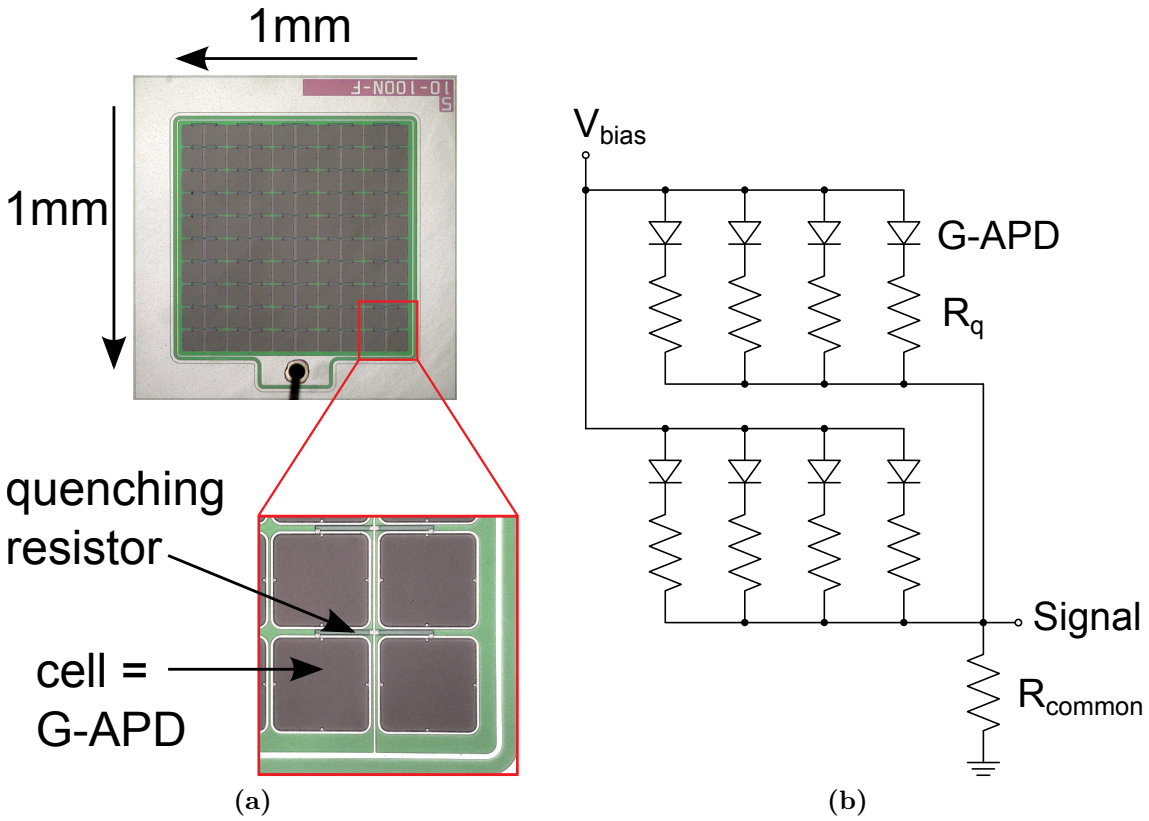

Figure 3.2: 3.2a: Image of an SiPM of 1x1 mm^2 size and 100 µm cell pitch. Taken from [16]. 3.2b: Schematic of SiPM array. Geiger-mode avalanche photodiodes are connected in series with quenching resistors R_q. Many of these photodiodes are in parallel to the bias voltage V_{bias} building up the array. Taken from [8].

Due to the maximal amplification of each detected photon, i.e. the operation of the SiPM in saturation range, the output signal is binary i.e. it can only be stated if a photon was detected or not (or rather if a cell breakdown occurred). To enable measurements showing a direct proportionality between output signal and number of cell breakdowns, G-APDs (with quenching resistor) are connected in parallel

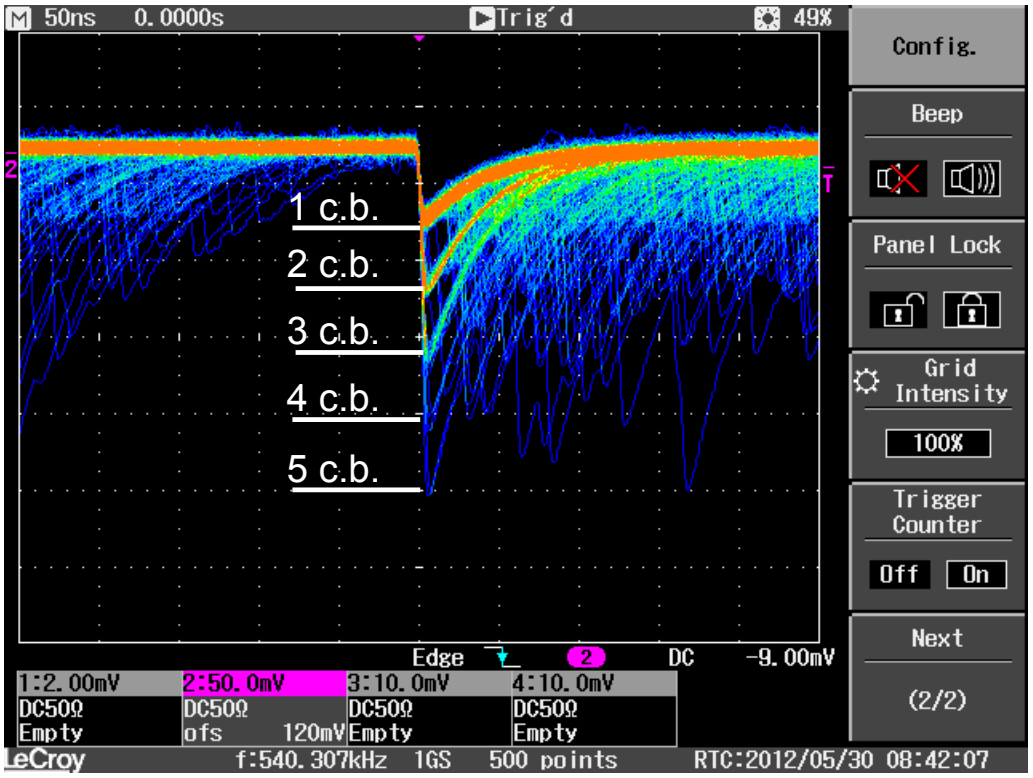

Figure 3.3: Oscilloscope screenshot of cell breakdowns (c.b.). A certain number of cell breakdown causes always the same pulse height.

(c.f. fig. 3.2). These arrays are the construction method of SiPMs with the G-APDs refered to as cells. An example of amplified SiPM signals is given in figure 3.3. The figure shows an oscilloscope screenshot with SiPM signals having different pulse heights. These are equivalent to the number of cell breakdowns. All pulse heights of a certain number of cell breakdowns are almost equally high and clearly distinguishable from the others, thus allowing to count photons. Small variances within the pulse high are due to gain fluctuations. The number of individual cells sets the limit of the dynamic range of an SiPM, since for the maximal flux all cells break down simultaneously and each cell can only detect one photon at once.

A crucial characteristic of an SiPM is the photon detection efficiency (PDE). It is given by

$$PDE = QE \cdot f_{\text{geom}} \cdot P_{\text{trigger}} \tag{3.2}$$

with QE being the quantum efficiency, f_{geom} the geometric fill factor and P_{trigger} the trigger probability. The quantum efficiency gives the probability of a photon to create an electron-hole pair. This quantity strongly depends on the mean free path length and therefore the wavelength of the photon. The geometric fill factor can reach values up to 80 %. It is limited due to the dead space caused by the resistors lying on top of the cells and trenches to suppress optical crosstalk (for an explanation of crosstalk see sec. 3.2.1). The trigger probability describes the

probability that electrons or holes trigger an avalanche. This value is close to 100 % if the over-voltage is adequate. Currently the PDE of SiPMs is close to the one of state-of-the-art PMTs which have an PDE of up to 35 % [17]. But improvements are strongly expected in the near future [15]. For example, it was already achieved to produce an SiPM with a PDE of (50-60) % in the wavelength range of $(350 - 500)$ nm [18].

3.2 Noise Phenomena of SiPMs

Cell breakdowns cannot only occur due to photon absorption but may also be caused by noise phenomena. The three components of noise phenomena are thermal noise due to thermal excitation, optical crosstalk caused by self emitted photons and after-pulses created by defects in the silicon lattice. Optical crosstalk and after-pulses are summarised as correlated noise [15].

3.2.1 Optical Crosstalk

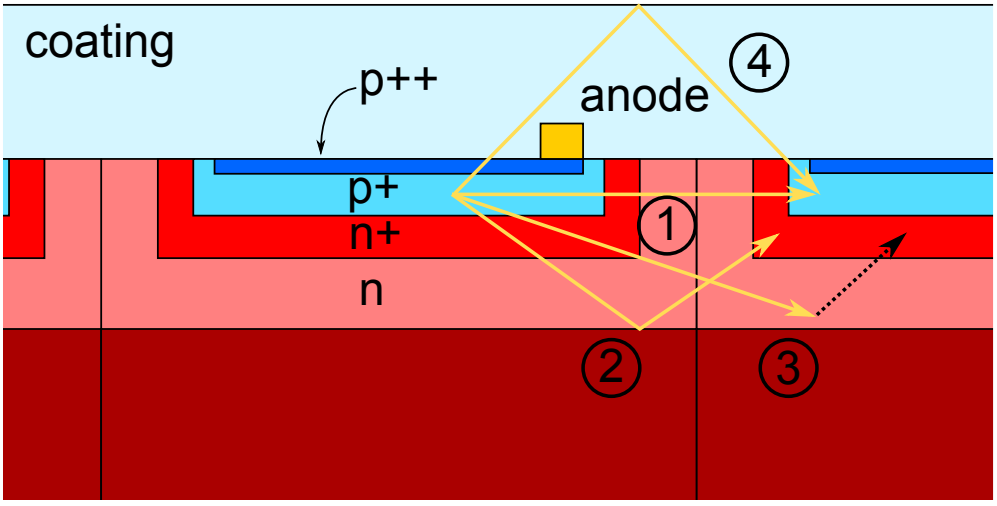

Figure 3.4: Schematic of optical crosstalk possibilities. 1) direct transmission, 2) internal reflection at boundaries, 3) creation of electron-hole pair and drift into depletion zone, 4) transmission through coating and reflection on boundary. Taken from [8].

During a cell breakdown a recombination of an electron with its counterpart may occur accompanied with the emission of a photon. This photon can trigger a cell breakdown in a neighbouring cell in four different mechanisms (cf. figure 3.4: direct transmission (1); internal reflections at boundaries into the neighbouring cell's depletion zone and absorption (2); creation of an electron-hole pair in n-doped region of neighbouring cell and drift into depletion zone (3); transmission through coating layer and reflection on coating boundary (4)). Again, it is not possible to distinguish between signal and crosstalk photon. The effect has been quantified in [19] for different SiPMs and is a function depending on the temperature and the over-voltage.

3.2.2 After-Pulses

The silicon lattice of the SiPM has imperfections. The electrons of the avalanche can get trapped and be released with delay, i.a. after the cell is recharged and therefore a new cell breakdown is triggered, refered to as after-pulse. After-pulses have as well been characterised in [19] for different SiPMs depending on the temperature and the over-voltage.

3.2.3 Thermal Noise

Electron-hole pairs can be generated thermally and start an avalanche process equal to signal photons. The cell breakdowns due to thermal noise are not distinguishable from cell breakdowns due to light.

Dark Counts

Additionally, a correlation between the three effects exists. Thermal noise and correlated noise can cause both after-pulses and optical crosstalk with the given probabilities. The noise effects in total increase with the number of cells i.e. SiPMs with many cells are more effected.

Since these noise effects occur regardless of the absorption of light photons, the rate measurable in total darkness is refered to as dark count rate. To quantify the rate caused by dark counts, measurements in total darkness are performed. For the Hamamatsu 3 x 3 mm^2 SiPM with a cell pitch of 100 μm (and therefore 900 cells) the average dark count rate has been determined to about $(4 - 5)$ MHz.

3.3 Signal Processing

The SiPM signal output is processed from analog to digital to enable further analysis. The single devices are described in this section.

3.3.1 SiPM Amplifier

The first device within the signal processing is used to amplify the signal. An amplifier board was designed by F. Beißel et al. and manufactured at III. Phys. Inst. B, RWTH Aachen University. This enables measurements with two different outputs: The fast output (FAST OUT) was intended for timing measurements whereas the integrating output (INT OUT) suits to energy measurements.

In this thesis both outputs are necessary. By measuring the dark rate with the INT OUT the over-voltage is determined (cf. chapter 5.2.6). The measurements for the analysis of the light flux are performed with the FAST OUT since the analysis algorithm works more reliable for this output (cf. sec. 5.1).

3.3.2 ADC - CAEN V1729

The amplified signal is transmitted into a analog-to-digital converter (ADC). One of the two ADCs used is the four channel flash analog-to-digital converter (FADC) CAEN V1729. It covers a dynamic range from $-500\,\mathrm{mV}$ to $+500\,\mathrm{mV}$ with a 12 bit resolution. Built-in is a circular memory with 2520 valid samples. Since the sampling frequency is either 1 GHz or 2 GHz, the resulting trace-length taken is either 2520 ns or 1260 ns [20]. For brightness measurements longer traces are beneficial and a time resolution of 1 ns is sufficient. Therefore, the 1 GHz sampling frequency has been chosen for all measurements.

Wiener VM-USB

The signal transmission between the FADC and a PC is ensured by the interface Wiener VM-USB [21].

LibLAB

To have an access to the laboratory hardware (FADC, Wiener VM-USB and Oscilloscope), i.e. read and write the output signals, an object orientated C++ interface, the LibLAB [22], was developed at III. Phys. Inst. , RWTH Aachen University.

3.3.3 ADC - Oscilloscope

Another ADC used within the measurements is the LeCroy Wavejet 354 A oscilloscope [23]. It can be controlled either by Ethernet connection or by USB. Sky scans are performed with the oscilloscope (cf. sec. 6.2.1) since a programme for the control of the telescope has already been written.

4. The Telescope

The SiPM together with the devices for signal processing, now refered to as SiPM light detection unit, are installed in the opening for the eyepiece of the telescope for brightness measurements of certain regions of the night-sky. Additionally, a light funnel in between SiPM and telescope simplifies the adjustment of position of the SiPM.

4.1 Technical Data

The used telescope type is a BRESSER Messier PN-203 210/1000 EXOS 2 manufactured by Meade. The optical design includes a spherical primary mirror to collect the incoming light. A secondary planar mirror diverts the light in direction of the opening for the ocular. This design is refered to as Newton reflector (cf. figure 4.1). The objective diameter measures 203 mm, the focal length f is 800 mm and the tube length is 700 mm.

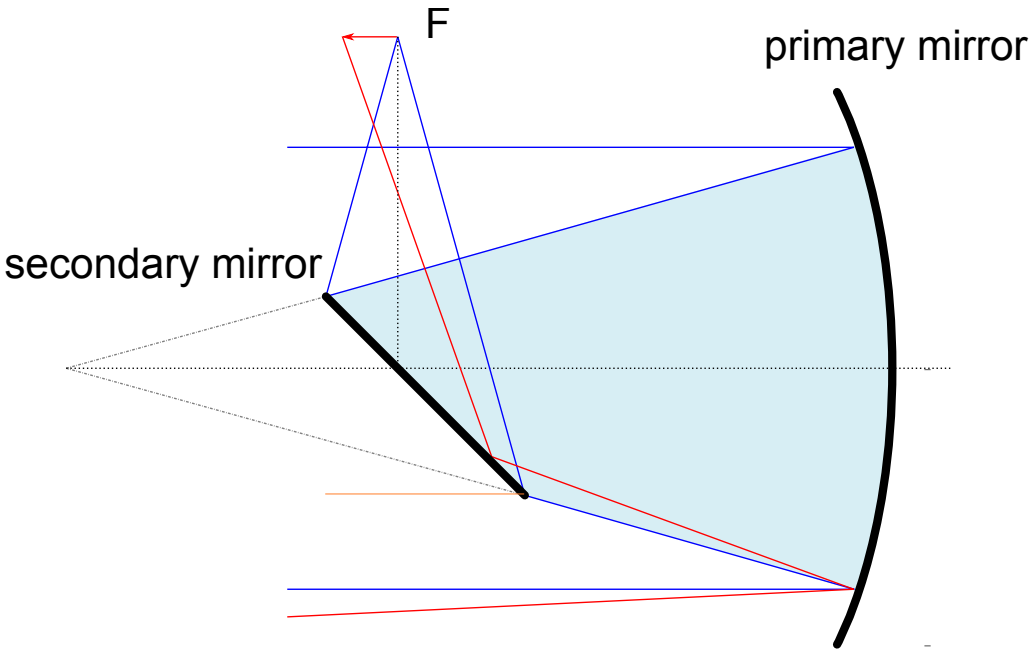

Figure 4.1: Schematics of a Newton reflector. The spherical primary mirror focuses the incoming light beam. The secondary planar mirror deflects the focused light beam in direction of the light detection unit. Adapted from [8].

4.2 One-Pixel-SiPM-Telescope

Instead of the eyepiece, allowing to observe the night-sky with the eyes, the SiPM light detection unit in addition to a light funnel (Winston cone) is mounted in the opening for the ocular. Consequently, the telescope has only one pixel.

Winston Cone

A special light funnel, reaching theoretically the maximum concentration, is the Winston cone which is used in this setup [24]. It is shaped parabolically with decreasing diameter from an entrance width of $d_{\text{Winston}} = (9.6 \pm 0.3)$ mm used here to an exit width of (3.0 ± 0.1) mm. The parabola is tilted by θ_{max} with reference to the symmetry axis. The exit point used for construction corresponds with the focal point which is on the opposite side of the exit. Consequently, all photons up to a maximal incident angle θ_{max} are accepted, the others leave the Winston cone again through the entrance. The Winston cone is due to construction a non-imaging light funnel. A high transmission is guaranteed by constructing the Winston cone out of polished aluminium. Aluminium oxidises on air influencing its reflectivity. This effect is studied in [25].

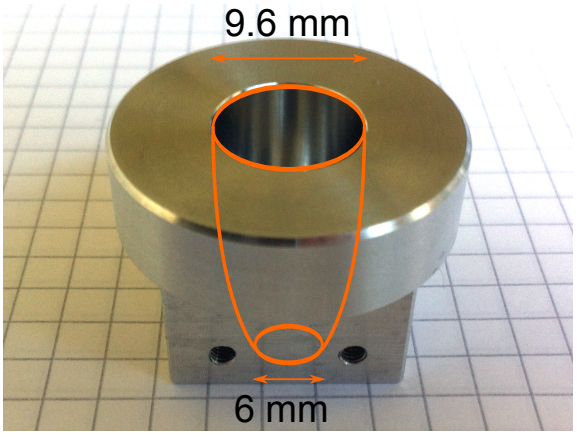

Figure 4.2: Photo of Winston cone made of aluminium. The thickness of the border has been adapted to the draw-tube of the Newton reflector. The Winston cone was constructed in the mechanical workshop of the Phys. Inst. III A, RWTH Aachen. Taken from [8].

The Winston cone increases the area onto which the light has to be concentrated. Therefore, focusing of the telescope is simplified since the Winston cone as non-imaging unit does not need to be placed exactly in the focal plane but only within a region in which the diameter of the light beam does not exceed the entrance width of the Winston cone (d_{Winston}). The length of this region (s) can be calculated using the intercept theorem (cf. fig. 4.3):

$$\frac{f}{d_{\text{objective}}} = \frac{s}{2 \cdot d_{\text{Winston}}} \tag{4.1}$$

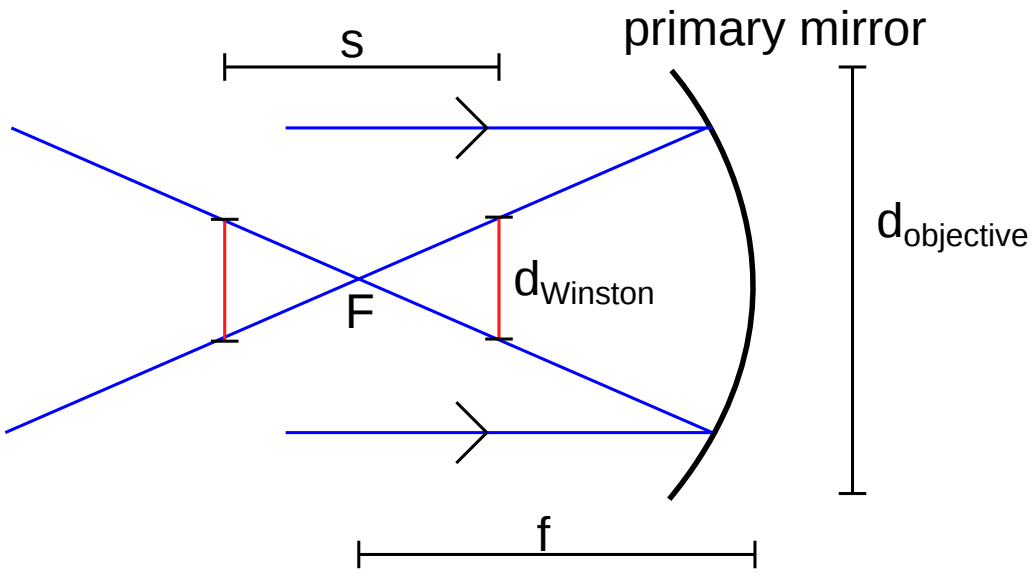

Figure 4.3: Focusing the Winston cone. The Winston cone can be mounted within a certain length s without light loss.

with f refering to the focal length and $d_{\text{objective}}$ describing the diameter of the objective. f, $d_{\text{objective}}$ and d_{Winston} are known so that s results to $s = (76 \pm 2)$ mm. The uncertainty is calculated with Gaussian error propagation for a variable having N uncorrelated uncertainties x_{i}:

$$(\Delta u)^2 = \sum_{\text{i}=1}^{N} \left(\frac{\partial u}{\partial x_{\text{i}}} \right) \sigma_{\text{i}}^2 \quad . \tag{4.2}$$

Although the region is relatively large, the focusing is performed with great awareness and accurateness to minimise photon loss.

Directly behind the Winston cone the SiPM is located. To stabilise the construction Winston cone, SiPM and amplifier board are built into a box. The SiPM is produced by HAMAMATSU (part number: S10362-33-100C [26])having a 100 µm cell pitch and a total size of 3 x 3 mm^2 covering the full exit area of the Winston cone. Consequently, there is no loss of photons due to construction.

Field of View

For brightness measurements it is essential knowing the field of view (FOV) for calculation of the light flux per solid angle unit. Geometrical considerations (cf. Figure 4.4) derive the formula for the calculation of the FOV:

$$\tan\left(\frac{\alpha_{\text{fov}}}{2}\right) = \frac{r_{\text{fp}}}{f} \tag{4.3}$$

with α_{fov} describing the aperture angle (FOV), r_{fp} the radius of the focal plane which is the greater radius of the Winston cone and f the focal length. Substituting

the values into equation (4.3) this leads to a maximal aperture angle of 0.69° with negligible error.

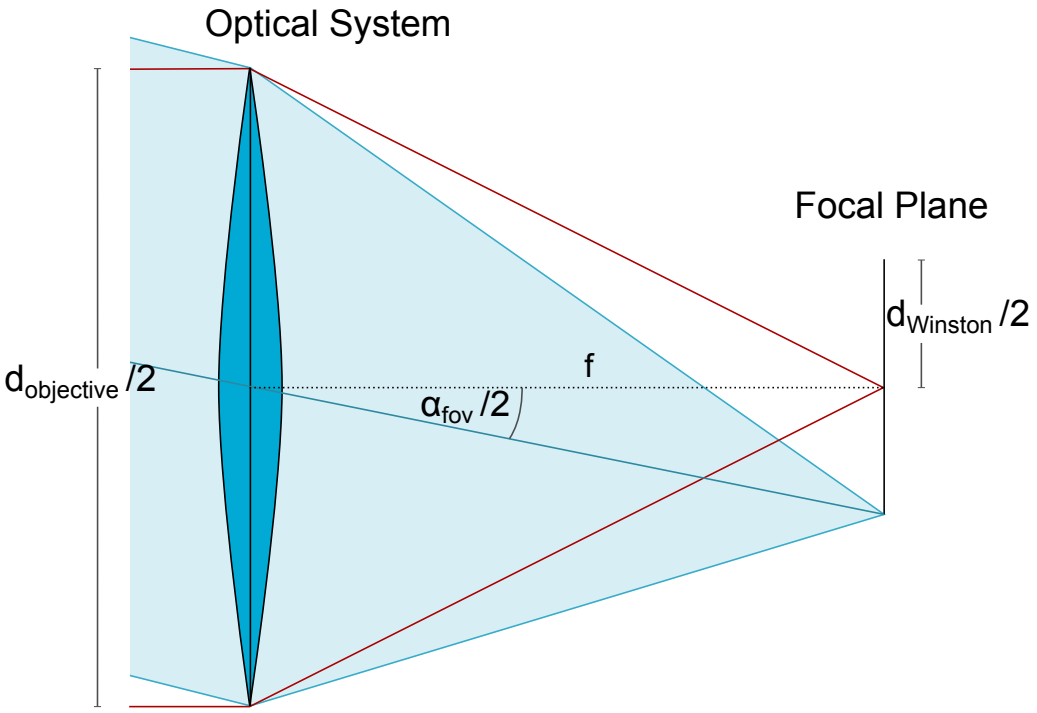

Figure 4.4: Geometric considerations for the calculation of the field of view α_{fov}. The optical system is in case of a Newton reflector a mirror that has the same effect as the convex lens. Adapted from [8].

Efficiency

Not only the field of view has to be considered but the efficiency of the telescope as well. To clarify the curve characteristics, the efficiency over the incident angle of the focused light beam is simulated with Geant4 [8] (cf. fig. 4.5). For the analysis one specific value for the efficiency and the aperture angle is needed. In regard of the steep decrease in the region between 0.69° and 0.73° representing the upper boundary of the FOV, the middle is chosen as value for further analysis. The value at the beginning of the steep decrease is equal to the calculation. The uncertainty is given by half the region: $\Delta\alpha_{\text{fov}} = 0.02°$. Consequently, the FOV is given as $(0.71 \pm 0.02)°$. The same procedure is used for the efficiency. With the efficiency falling slightly in the region between 68 % and 58 %, the mean efficiency is $(63 \pm 5)\,\%$.

The efficiency of the Winston cone and SiPM complex is not needed as the same components are used for FAMOUS and can therefore be regarded as part of the pixel.

4.3 Stellarium

Stellarium is an open source planetarium. It enables i.a. an easy telescope control. A default catalogue of over 600,000 stars plus images of nebulas, planets and a

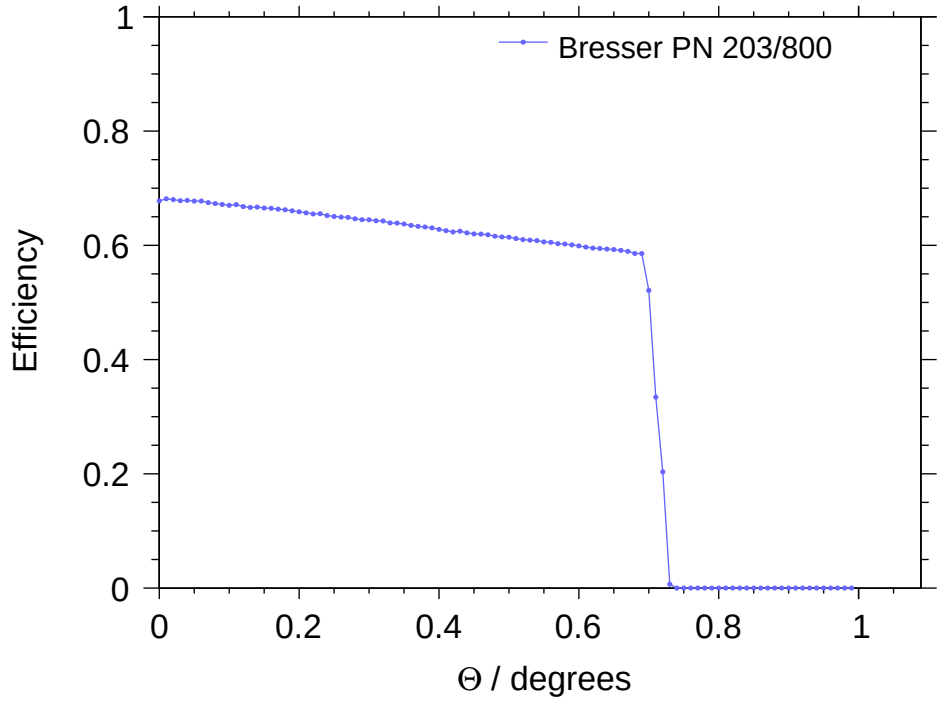

Figure 4.5: Efficiency of the telescope simulated with Geant4. The efficiency decreases strongly in the region of 0.69° to 0.73° which is the upper boundary of the field of view. Picture credit: M. Stephan, RWTH Aachen University

realistic image of the milky way reflect the night-sky with bright and dark regions [27]. Consequently, dark regions can be determined and steered for with the telescope for measurements.

4.4 INDI

For the communication between telescope and PC the INDI server is used which is the standard for the control of astronomical equipment. INDI was developed by Elwood C. Downey of ClearSky Institute and stands for Instrument-Neutral-Device-Interface. It is a protocol which supports not only the control among hardware devices and software frontends but also automation, data acquisition and exchange among them [28].

5. Light Flux Calculation

The data taken with the one-pixel-silicon-photomultiplier telescope is analysed in C++ using the data analysis framework ROOT [29]. The light flux is calculated and correction terms and their uncertainties are considered. Besides crosstalk, afterpulses and thermal noise (which is fully included in dark counts), these corrections are dead time effects of the silicon-photomultiplier (SiPM), a correction term for the used algorithm itself and the efficiency of the telescope.

5.1 Light Flux

The measurements for determining the light flux of stars and the night-sky are taken with the FADC (cf. sec. 3.3.2). An example of the recorded traces is given in fig. 5.1. The voltage of the SiPM output is recorded over the time. Cell breakdowns are dips within the voltage trace. In general, the amplitude stands in direct proportion to the number of cell breakdowns. For equal number of cell breakdowns the amplitudes have approximately the same magnitude (cf. fig. 3.3). The number of cell breakdowns in turn is of interest due to the proportionality to the light flux.

A phenomenon observable in the FADC traces is the pile-up of pulses. Since only the time for the voltage decrease after a cell breakdown is short but not the recovery time, another cell breakdown may occur during this period of time in a different cell. If so, although the amplitude is not affected, the absolute dip voltage (i.e. the minimal voltage after a cell breakdown) is deeper than the one of a cell breakdown while the array is fully recharged. It may also occur that the same cell breaks down within its own recovery time. As a result, in case of the fast output (FAST OUT) the amplitude of the second pulse is only slightly smaller but in case of the integrating output (INT OUT) the amplitude is effected strongly. Therefore, a simple threshold scan cannot be applied.

Besides the pile-up effect, the amplification chain picks up noise which has to be distinguished from the SiPM signals. The characteristics of this noise effect are fast oscillating amplitudes around the baseline.

To avoid the problem of the pile-up effect, not the curve of the trace itself is used but voltage differences between two certain points[1]. The aim of the analysis is to find the dips within the traces. The minimal time distance between the points is a defined time window of 3 ns. In case of a decrease in voltage within this time

[1] The analysis algorithm to find cell breakdowns is taken from [19].

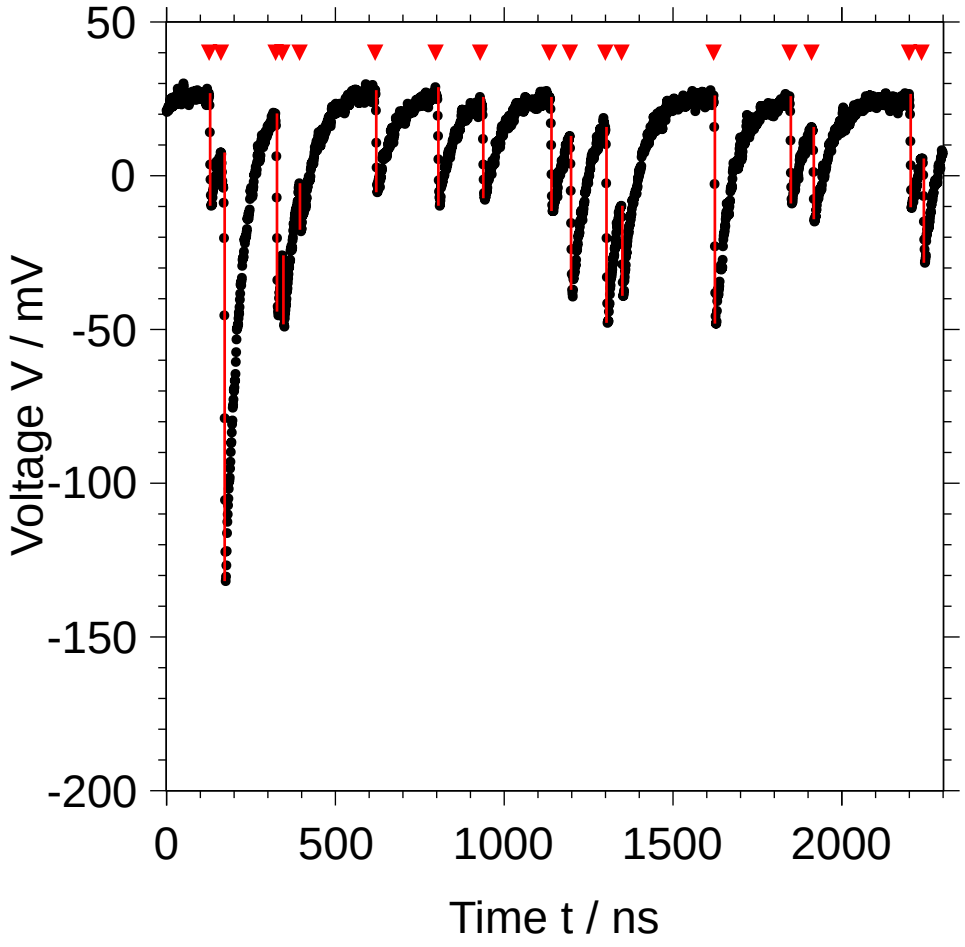

Figure 5.1: Example of a voltage trace measured by FADC. The dips are caused by the cell breakdowns of the SiPM. The red lines were added by the algorithm at the time of each cell breakdown. The length of the lines is equal to the amplitude of the pulses. The red triangles mark the time of the cell breakdowns.

interval, the starting points is marked. The whole time window moves forward in time until the last data point within the decrease is identified as dip minimum and therefore ending point. The voltage at the ending point is subtracted from the one at the starting point resulting in positive differences for dips in the traces. Since there is no further interest in the increasing parts of the traces, in case of increasing voltages the voltage differences within the time window itself is taken and there is no search for peaks. An important reason for the implementation of a time window is the hereby existing time threshold preventing fast oscillating noise to end the search of the dip prematurely. The resolution of signal peaks is not influenced through this.

The voltage differences are determined and written into a new histogram. An example can be found in fig. 5.2.

A peakfinder is applied to the histogram involving a threshold to suppress the noise due to amplification. Both time and amplitude of the cell breakdown are determined.

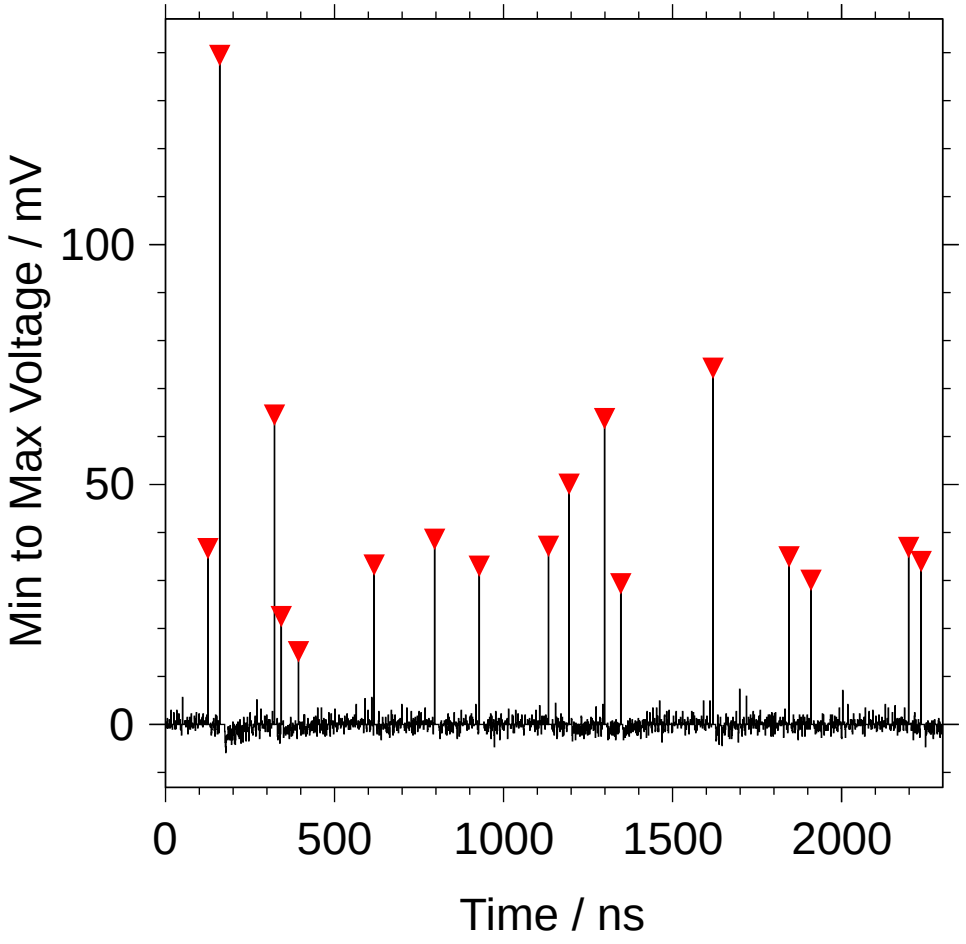

Figure 5.2: Histogram showing the voltage differences between maxima of the baseline and minima in the traces. The red triangles mark the time and the amplitudes of the dips found by the analysis after applying a voltage threshold to reduce the noise.

The value of the noise threshold has been varied and the effects have been studied to determine the value giving best results. It may neither be too small to prevent noise to pass the threshold nor be too high to ensure all signal pulses pass the threshold. By studying the effects in the voltage difference histograms an optimal value of 14 mV for the used settings was found, corresponding to approximately 44 % of the one photon pulse height for the FAST OUT.

The threshold for the INT OUT is smaller due to the phenomenon of small amplitudes if cell breakdowns occur during the recovery time. Noise is less distinctive as well causing no problem with smaller values. But studying the accuracy of identifying all cell breakdowns revealed some problems. Due to the integration pulses are melted to one and not all pulses of equal number of cell breakdowns have the same sized amplitude. This requires different data propagation (i.e. different corrections on the algorithm, cf. sec. 5.2) between the outputs of INT and FAST OUT.

As the FAST OUT will be used within the FAMOUS telescope, only this output is used within this thesis.

Finger Spectrum

Since time intervals without cell breakdowns are needed within the further analysis, the traces are divided into sections refered to as gates. To get most accurate results, high statistics are needed, i.e. high numbers of intervals without cell breakdowns and consequently of intervals in total. In principle, this is achieved for fine resolutions, i.e. with gate-widths close to the sampling rate which is equivalent to a gate-width of 1 ns. Consequently, a small value is likely to be chosen. But as one criterion to suppress the contribution of noise to the light flux was to test on fast oscillating amplitudes around the baseline (using the time window), the gate-width may not be arbitrary small. The optimal gate-width results to be 5 ns.

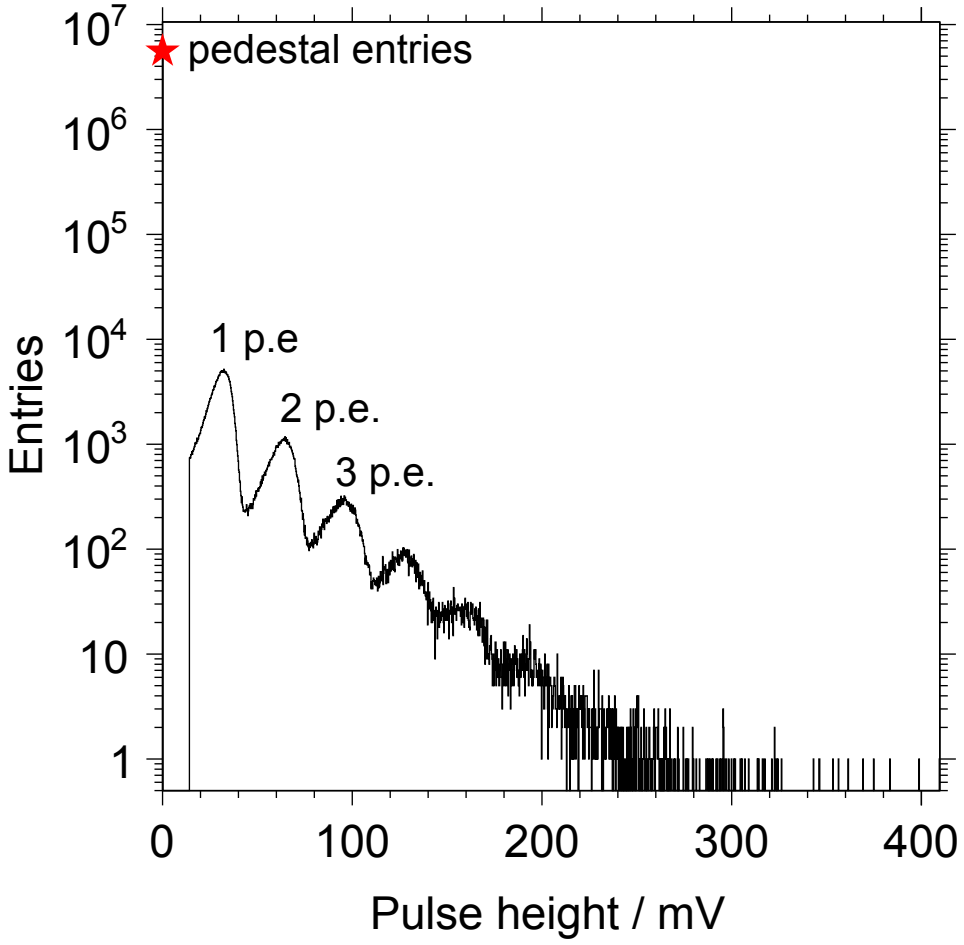

Figure 5.3: Example of a finger spectrum. The red star symbolises the number of pedestal entries. The fingers are refered to as photon equivalents (p.e.) peaks.

The time information of the peaks enables their allocation into a gate. All amplitudes (i.e. voltage differences) of the pulses of a gate higher than the noise threshold are summed up and written into a new histogram. This is repeated with all gates of

all traces of a measurement. The resulting histogram is called finger spectrum due to the fingers representing the peaks of a certain number of cell breakdowns. An example is shown in fig. 5.3. Since not only photons can cause cell breakdowns but also correlated and thermal noise, the peaks are refered to as photon equivalents (p.e.) peaks. The empty gates, i.e. the gates without peaks higher than 14 mV are counted and the number is written into the first bin of the histogram. This entries are refered to as pedestal entries.

Poissonian Mean

To calculate the light flux the finger spectrum is used[2]. For an ideal SiPM it follows a Poisson distribution. Therefore the probability density function of X, $P_\mu(X = N)$, is given by

$$P_\mu(X = N) = \frac{\mu^N}{N!} \cdot \mathrm{e}^{-\mu} \tag{5.1}$$

with μ being the expected value and the variance, X the discrete stochastic variable and N the number of p.e. of interest.

The parameter of interest representing the light flux is the expected value μ. To calculate μ the probability mass function is evaluated at N = 0:

$$P_\mu(X = 0) = \mathrm{e}^{-\mu} \quad , \tag{5.2}$$

$P_\mu(X = 0)$ can also be express with the pedestal entries N_{ped} and the total number of entries N_{tot}:

$$P_\mu(X = 0) = \frac{N_{\mathrm{ped}}}{N_{\mathrm{tot}}} \quad . \tag{5.3}$$

Combining equations (5.2) and (5.3) results in

$$\mu = -\ln\left(P_\mu(X = 0)\right) = -\ln\left(\frac{N_{\mathrm{ped}}}{N_{\mathrm{tot}}}\right) \quad . \tag{5.4}$$

The light flux f_{Poisson} is the expected number of photons per time interval. Therefore, μ has to be divided by the time to which it relates, in this case the gate-length t_{gate}, resulting in

$$f_{\mathrm{Poisson}} = \frac{\mu}{t_{\mathrm{gate}}} \quad . \tag{5.5}$$

[2]The method using the Poissonian mean is taken from [30]

Calculating the light flux with the method using the Poisson mean, the statistical uncertainty of $P_\mu(X = 0)$ is given by the binomial error [31]

$$\sigma_{\mathrm{P}(\mu,0)} = \frac{1}{N_{\mathrm{tot}}} \cdot \sqrt{N_{\mathrm{tot}} \cdot \mathrm{P}(\mu, 0) \cdot (1 - \mathrm{P}(\mu, 0))} \tag{5.6}$$

since every gate can be classified as part of N_{ped} or not, enabling the description as Bernoulli experiment. With Gaussian error propagation (cf. eq. (5.1)) the uncertainty of the light flux f_{Poisson} is determined.

The SiPM used is not an ideal detector without any noise, but the analysis algorithm corrects on all noise effects affecting N_{ped} and N_{tot} (cf. sec. 5.2). Therefore, this method is adequate for the analysis.

As already mentioned above, several correction terms and their uncertainties have to be taken into account. The implementation of these into the analysis is described in the following section.

5.2 Correction Terms and Uncertainties

It is essential to implement the correction terms in the right order. The order of these and the used algorithm are explained further on.

5.2.1 Optical Crosstalk

Optical crosstalk events (cf. sec. 3.2.1) occur simultaneously to another cell breakdown and therefore never as single pulses. This especially means that optical crosstalk does not change the number of pedestal entries. As the light flux calculation method uses only the number of counts in the pedestal and the total number of cell breakdowns, the rate is already corrected on optical crosstalk. This has to be taken into account in further correction steps.

5.2.2 Corrections on Algorithm

The second correction done is the correction of the algorithm to find the cell breakdowns and create the finger spectrum. The algorithm does not find all the cell breakdowns of the SiPM array. Therefore, a Monte Carlo simulation has been performed by M. Stephan, RWTH Aachen University, to determine the deviation from the actual amount of cell breakdowns[3]. The curve can be found in fig. 5.4.

The algorithm has to be corrected right at the beginning (i.e. the first correction implemented in the algorithm) for all the other correction terms base on the real number of cell breakdowns. This procedure achieves a calculation of the light flux with sensible physical variables not dependent on the algorithm.

[3]based on a software developed by T. Niggemann et al. with Geant4 [7]

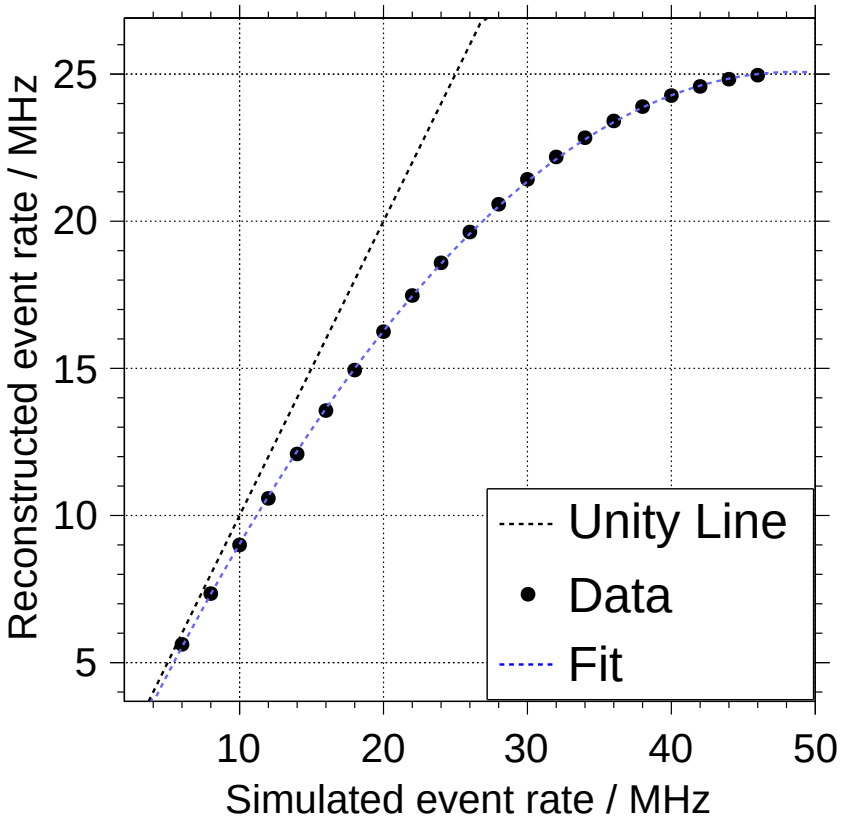

Figure 5.4: Monte Carlo Simulation for Corrections on algorithm. Picture credit: M. Stephan, RWTH Aachen University. Simulation up to 50 MHz. The uncertainty due to the fit is negligible in comparison to the other uncertainties within the analysis.

The curve of the Monte Carlo simulation can be parameterised by a polynomial of second degree with three fit parameters p_0, p_1 and p_2

$$f_{\text{Poisson}} = p_0 + p_1 \cdot f_{\text{MC}} + p_2 \cdot f_{\text{MC}}^2 \tag{5.7}$$

The light flux calculated with the Poissonian mean is f_{Poisson} and is corrected to f_{MC} with [32]

$$f_{\text{MC}} = -\sqrt{\left(\frac{p_1}{2 \cdot p_2}\right)^2 - \frac{p_0}{p_2} + \frac{f_{\text{Poisson}}}{p_2}} - \frac{p_1}{2 \cdot p_2} \quad , \tag{5.8}$$

with $p_0 = -0.37$, $p_1 = 1.05$ and $p_2 = -0.01$.

The simulation is only well-defined for reconstructed rates smaller than 24 MHz (cf. fig. 5.5) since thereafter it is not possible to find an explicit inverse function. Therefore, the analysis is stopped for higher light fluxes. The uncertainty due to the fit is negligible in comparison to the other uncertainties within the analysis.

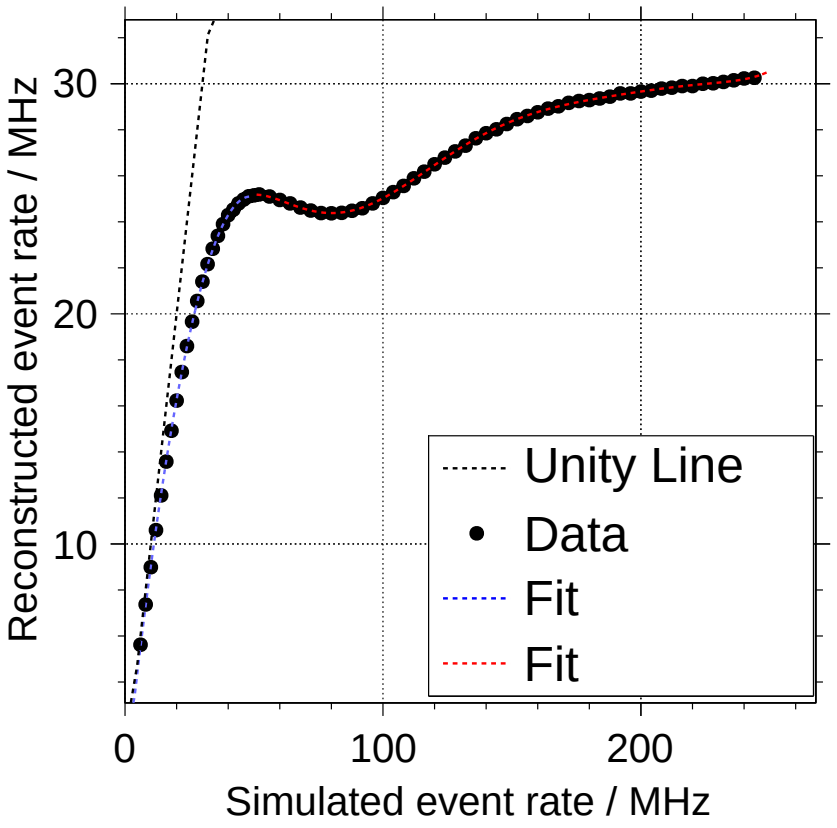

Figure 5.5: Monte Carlo Simulation for Corrections on algorithm. Picture credit: M. Stephan, RWTH Aachen University. Whole simulation showing that only the range below 24 MHz of the simulated event rate is well-defined. The uncertainty due to the fit is negligible in comparison to the other uncertainties within the analysis.

The uncertainty of the Monte Carlo simulation has been determined to $\sigma_{\mathrm{MC}}^{\mathrm{sys}} = 0.0045 \cdot f_{\mathrm{MC}}$ [32]. Since all light flux values are corrected in the same direction and about the same value the uncertainty is treated as systematic uncertainty.

The binomial error of the light flux calculation is statistical and is propagated via Gaussian error propagation (cf. eq. (5.1)).

5.2.3 Dead Time Effects

The single cells of the SiPM are not sensitive all the time. After a cell breakdown the cell has to be recharged. The time needed to get back into the initial state is called recovery time t_{rec}. During a certain time within this recovery time, the cell cannot detect further photons. This time is refered to as dead time t_{dead}.

The dead time of the SiPM used has so far not been determined. But the recovery time was studied in [33] and it was found to be $(46.9 - 48.9)$ ns. For the analysis the maximal value is used to estimate the maximal effect dead time can have because $t_{\mathrm{dead}} < t_{\mathrm{rec}}$. An uncertainty of 10 ns downwards is set to portray the contribution of

the dead time and clarify whether it is essential to know the exact dead time or the estimation with the recovery time is sufficient.

The basic idea for this correction is to determine the sensitive time and divide the number of photon equivalences (p.e.) not by the total measuring time but by the sensitive time.

The total sensitive time depends on the number of cell breakdowns during the measurement. Many cell breakdowns imply a longer total dead time and therefore a shorter total sensitive time. Consequently, the correction on dead time effects has to be implemented before further corrections are taken into account since the dead time only depends on the total number of cell breakdowns of each measurement.

Additionally, after-pulses during the dead time are not possible. But when correcting for the dead time effect, it is implicitly assumed that cell breakdowns do not cause dead time and consequently no after-pulses can be suppressed. Therefore, one possibility would be to determine the additional number of after-pulses in case of no dead time and add the rate due to these (by dividing the number of these after-pulses by the dead time). Within this analysis another method is chosen. As later on all after-pulses have to be subtracted from the cell breakdowns, including i.a. the additional after-pulses, this part of the correction is brought forward and the after-pulses are not added.

The sensitive time t_s is calculated with

$$t_\mathrm{s} = t_\mathrm{total} - t_\mathrm{dead}^\mathrm{total} \tag{5.9}$$

with t_total being the total measuring time and $t_\mathrm{dead}^\mathrm{total}$ the total dead time. The total dead time is the sum of all single dead times after cell breakdowns and related to one cell. At this point one has to consider the cell breakdowns caused by optical crosstalk which the analysis already accounts for. For the total dead time calculation these pulses have to be taken into account. Any pulse may cause an optical crosstalk event with the probability P_CT and each crosstalk event can be the source of another crosstalk event, too. This is considered by implementing an infinite sum over the crosstalk probability P_CT (the value is determined in sec. 5.2.6). With N_pe being the number of photon equivalences after the algorithm correction, the total dead time can be calculated with

$$t_\mathrm{dead}^\mathrm{total} = t_\mathrm{dead} \cdot \frac{N_\mathrm{pe} \cdot \sum_{n=0}^{N} {P_\mathrm{CT}}^n}{N_\mathrm{cells}} = t_\mathrm{dead} \cdot \frac{N_\mathrm{pe}}{N_\mathrm{cells} \cdot (1 - P_\mathrm{CT})} \quad . \tag{5.10}$$

By dividing by the number of cells N_cells it is taken into account that the total time and the dead time are both in relation to one cell and not to the complete array.

Consequently, the rate is calculated with

$$f_{\mathrm{DT}} = \frac{N_{\mathrm{pe}}}{t_{\mathrm{s}}} \quad . \tag{5.11}$$

Uncertainties

Since the dead time has to be estimated with the recovery time, the resulting rate is systematical too high. The systematic uncertainty is given by the difference between the rate calculated with the maximal value for the dead time $t_{\mathrm{dead}} = t_{\mathrm{rec}} = 48.9\,\mathrm{ns}$ and the rate calculated with the above explained 10 ns subtracted. Since the crosstalk probability P_{CT} contributes as well to the uncertainty, the minimal value P_{CT} within its uncertainty is implemented in the calculation together with the minimal dead time to calculate the maximal uncertainty.

The systematic uncertainty due to the Monte Carlo simulation is propagated in the same way as the uncertainty due to dead time is determined: The Monte Carlo uncertainty is added to the rate before the dead time correction and implemented into eq. (5.11). The absolute difference to the value calculated without added uncertainties is taken as uncertainty.

The statistical uncertainty is again propagated with Gaussian error propagation.

The results demonstrate that the uncertainty caused by t_{dead} is only very small in comparison to the other uncertainties (cf. chapter 6). Therefore, the estimation with the recovery time can be used since changes within the time result to have little impact.

5.2.4 After-Pulses

The next correction term of the light flux rate caused by the method of detection (with SiPMs) is the correction for after-pulses. At this point of the analysis the number of photon equivalences is composed of the detected photons, after-pulses and dark counts. By subtracting the after-pulses from this number the rate of the night-sky and stars without any noise effects is calculated. As explained before, no after-pulses were added within the dead time correction and therefore these do not have to be subtracted here. The method to subtract the remaining after-pulses used in this algorithm is to make use of the after-pulse probability P_{AP}. In sec. 3.2.2 it was pointed out that after-pulses might be caused by all pulse types, i.e. optical-crosstalk events cause after-pulses with the same probability as light pulses or even after-pulses themselves do. Therefore, the first step within this correction is to determine the average number of after-pulses caused by one light pulse. This includes all after-pulses of optical crosstalk events and previous after-pulses whose origin is the light pulse event. A graphical explanation can be found in fig. 5.6.

To calculate the average number of pulses, all possibilities of crosstalk and after-pulses are summed up, each weighted with the probability of occurance. For a certain number of crosstalk events m and after-pulses n there exist $(n+m)!$ possible ways to order these. If every sequence (with a sequence refering to a defined combination

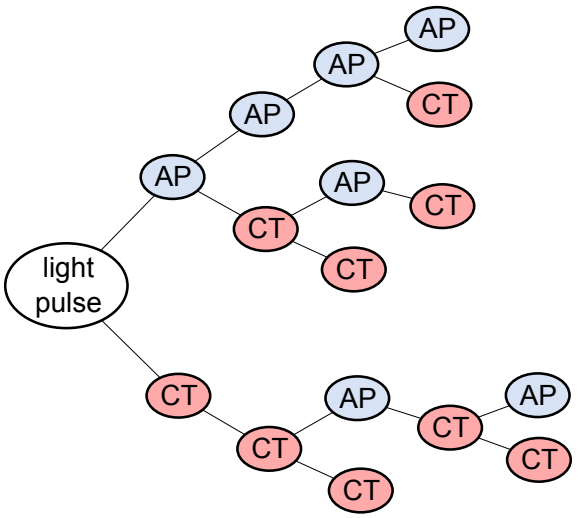

Figure 5.6: Selection of possible branches of crosstalk events (CT) and after-pulses (AP) arose from a light pulse, refered to as sequences. The probability for each cell breakdown due to a noise effect at the end of a branch, or rather the average number of occurrance after a light pulse of this event, is given by the multiplication of probabilities of the preceding effects.

of after-pulses and crosstalk events) may only be counted once one has to divide it by $n! \cdot m!$. The average number of occurrance of n after-pulses (m crosstalks) after a light pulse is included by multiplying m (n) times with the probability of after-pulses (optical crosstalk). As the number of crosstalk events and after-pulses is unknown, two infinite sums are included. Finally, this leads to the number of total after-pulses and crosstalk events $N_{\mathrm{AP+CT}}$

$$N_{\mathrm{AP+CT}} = \sum_{n=0}^{\infty} \sum_{m=0}^{\infty} \frac{(n+m)!}{n! \cdot m!} \cdot (P_{\mathrm{AP}})^n \cdot (P_{\mathrm{CT}})^m \quad . \tag{5.12}$$

The summand $n = m = 0$ is allowed meaning that the pulse itself is included in this sum as well. As only the number of after-pulses plus the light pulse is of interest, the number of crosstalk events has to be subtracted of this sum. Thus, all sequences ending on crosstalk are subtracted since these give the probability for such an event and therefore its average number of occurrance after a light pulse. The number of these events ending on crosstalk can be calculated similarly with

$$N_{\mathrm{CT}} = \sum_{n=0}^{\infty} \sum_{m=1}^{\infty} \frac{(n+(m-1))!}{n! \cdot m!} \cdot (P_{\mathrm{AP}})^n \cdot (P_{\mathrm{CT}})^{m-1} \cdot P_{\mathrm{CT}} \tag{5.13}$$

$$= \sum_{n=0}^{\infty} \sum_{m=0}^{\infty} \frac{(n+m)!}{n! \cdot m!} \cdot (P_{\mathrm{AP}})^n \cdot (P_{\mathrm{CT}})^m \cdot P_{\mathrm{CT}} \tag{5.14}$$

as the last part of the sequence is now fixed. Substracting this term of eq. (5.12) the number of after-pulses plus light pulse results to be

$$N_{\mathrm{AP}} = \sum_{n=0}^{\infty} \sum_{m=0}^{\infty} \frac{(n+m)!}{n! \cdot m!} \cdot (P_{\mathrm{AP}})^n \cdot (P_{\mathrm{CT}})^m \cdot (1 - P_{\mathrm{CT}}) \quad . \tag{5.15}$$

The after-pulse probability P_{AP} may not include the suppressed after-pulses during dead time effects. This probability was measured in [19] as function of the over-voltage. The value needed here is determined in sec. 5.2.6.

Finally, the light flux rate can now be corrected on after-pulses by dividing the rate calculated so far by the average number of after-pulses plus the light pulse itself:

$$f_{\mathrm{AP}} = \frac{f_{\mathrm{DT}}}{N_{\mathrm{AP}}} \quad . \tag{5.16}$$

Uncertainties

The probabilities for optical crosstalk P_{CT} and after-pulses P_{AP} are both quantities with uncertainties. These define the uncertainty of f_{AP}. It is asymmetric and calculated by implementing first the maximal probabilities and second the minimal probabilities within the uncertainties into eq. (5.16).

Systematical and statistical uncertainties from previous correction steps are propagated the same way as before.

5.2.5 Efficiency of Telescope

Besides the correction terms implemented due to the light collection with SiPMs, the efficiency of the telescope has to be considered as well. The corresponding curve is shown in fig. 4.5. An average value for the analysis of $\epsilon = 0.63 \pm 0.05$ was determined. To correct on the lost photons due to the efficiency of the telescope, the light flux rate after the after-pulse correction is divided by it

$$f_{\epsilon} = \frac{f_{\mathrm{AP}}}{\epsilon} \quad . \tag{5.17}$$

The uncertainty of the efficiency is propagated by implementing the minimal (maximal) value within the uncertainty into eq. (5.17). The difference to the value calculated before is the systematic uncertainty due to the accuracy of the efficiency.

The other systematic uncertainties are propagated in the same way as before. The statistical uncertainty is propagated with Gaussian error propagation.

5.2.6 Determination of the After-Pulse and Crosstalk Probability

To complete the analysis algorithm, the probability of after-pulses and optical crosstalk has to be determined. Within [19], the after-pulse and crosstalk probabilities in dependency of the over-voltage V_{OV} were measured. Consequently, the over-voltage has to be known.

The over-voltage can be determined by measuring the one p.e. pulse peak-voltage of the fast output of the SiPM amplifier in dependency of the bias-voltage V_{b} (cf. fig. 5.7). A finger spectrum of a measurement taken with this output can be found in fig. 5.3. The maximum of the one p.e. peak differs with the temperature. This can be observed by comparing data over different days and times of the night. Consequently, all one p.e. finger spectrum peaks of the dark count measurements have to be analysed. The uncertainty is determined by fitting a Gaussian function on each peak. In the example in fig. 5.3 the 1 p.e. voltage is at $(37.0 \pm 0.5)\,\mathrm{mV}$.

The breakdown voltage U_{BD} is the y-intercept. It is determined to $U_{\mathrm{BD}} = 69.6\,\mathrm{V}$ with negligible uncertainties. With eq. (3.1) the over-voltage can be calculated with the knowledge of the bias voltage and the breakdown voltage of the measurements shown in fig. 5.7. Consequently, the over-voltage can be determined with the 1 p.e. pulse voltage at any temperature and the uncertainties are propagated. For the example this results in $(1.31 \pm 0.03)\,\mathrm{V}$ (cf. fig. 5.7). All over-voltages lie within the range of $1.1 - 1.3\,\mathrm{V}$.

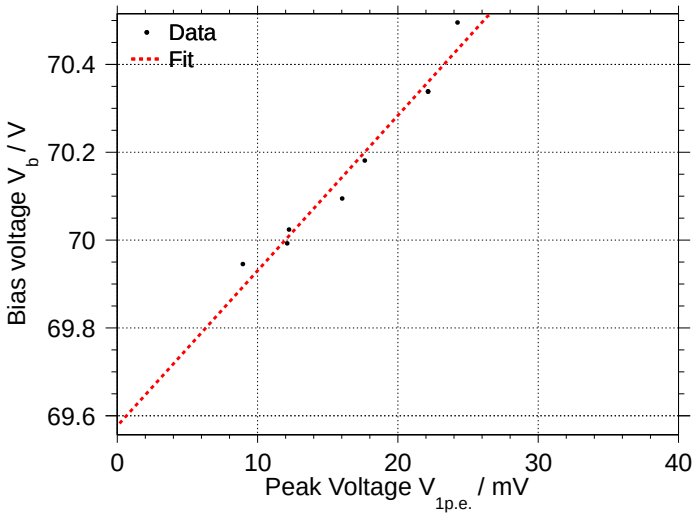

Figure 5.7: Determination of the over-voltage V_{ov}. With the knowledge of the bias voltage and breakdown voltage of the SiPM, the over-voltage can be determined out of eq. (3.1). Picture credit: M. Stephan, RWTH Aachen University.

Finally, the probabilities can be read from the curves to be found in [19]. They vary in the range of $P_{\mathrm{CT}} = (19 - 27)\,\%$ and $P_{\mathrm{AP}} = (20 - 31)\,\%$. In the example they result to be $P_{\mathrm{CT}} = (27.0 \pm 1.5)\,\%$ and $P_{\mathrm{AP}} = (31 \pm 3)\,\%$.

5.2.7 Dark Counts

Cell breakdowns are not only caused by photons but also by thermal excitation and the following correlated noise, together known as dark noise (cf. 3.2.3). The dark rate ($f_{\mathrm{dt}}^{\text{dark noise}}$) is measured in regular intervals and subtracted from measurements of stars and the background luminosity (f_{dt}^{s+b}). The analysis corrects only non dark noise measurements with

$$f_{\mathrm{DC}} = f_{\mathrm{SI}}^{\mathrm{s+b}} - f_{\mathrm{SI}}^{\text{dark noise}} \quad . \tag{5.18}$$

Uncertainties

The rates of both dark count measurements and star or night-sky measurements deviate within their systematic uncertainties in the same direction. Therefore, the systematic uncertainties from dark count measurements and star or night-sky measurements are subtracted from each other and the absolute values are the new systematic uncertainties after the dark count correction. Here it is assumed that the uncertainties are 100% correlated.

The statistical uncertainty is propagated with Gaussian error propagation.

5.3 Conversion into SI-units

So far, the light flux was refered to as a certain number of photons depending on a time interval. But besides the information about the time during which data was taken, the solid angle and the entrance surface size of the telescope have to be indicated. As during all measurements the same telescope was used, this information includes always the same values. The entrance surface size $A_{\text{objective}}$ is

$$A_{\text{objective}} = \pi \cdot \left(\frac{d_{\text{objective}}}{2}\right)^2 \quad . \tag{5.19}$$

The solid angle Ω depends on the field of view (α_{fov}) (cf. sec. 4.2) and its unit is steradian (sr). It can be calculated with

$$\Omega = 4\pi \sin^2\left(\frac{\alpha_{\text{fov}}}{4}\right) \quad . \tag{5.20}$$

Finally, the light flux can be converted into SI-units with

$$f_{\mathrm{SI}} = \frac{f_{\mathrm{AP}}}{A_{\text{objective}} \cdot \Omega} = f_{\mathrm{AP}} \cdot (2.2 \pm 0.1) \cdot 10^5 \frac{1}{\mathrm{m}^2\ \mathrm{sr}} \quad . \tag{5.21}$$

Each uncertainty is propagated into the calculation of the light flux (cf. eg. (5.21)).

6. Brightness of Stars and the Night-Sky

All data taken, except the measurements performed with the oscilloscope, is analysed with the algorithm described in chapter 5. The first issue of interest was to demonstrate that distinction between stars and background light with the one-pixel-silicon-photomultiplier telescope is possible. Furthermore, measurements of the night-sky brightness have been performed. The effects of the UV-pass filter has been studied within these measurements. Additionally, data was taken at two sites with different contribution of light pollution, allowing a rough estimation of the effect in Aachen. Besides background light measurements, the light flux of stars was determined as well, thus enabling a calibration of the telescope.

6.1 Experimental Setup

The different parts of the experimental setup were already described in previous chapters (cf. chapter 3 and 4) except the UV-pass filter. Fig. 6.1 shows the schematics of the setup explaining the ways of signal and communication and figure 6.2 shows a photo of the setup. The UV-pass filter is described in the following section.

6.1.1 UV-Pass Filter

To perform brightness measurements with SiPMs, UV-pass filters are not essential but they have benefits regarding the purposes of this thesis. This is to be explained further on.

In general, the issue of interest is to detect the night-sky brightness photons which occur as background for FAMOUS. A small rate due to background is desirable to clearly distinguish between signal and background. Consequently, the first and most evident reason for using a UV-pass filter is to prevent photons due to night-sky brightness from reaching the SiPM and therefore being detected. Especially photons due to light pollution have wavelengths above the range of the UV-region and can consequently not pass the filter. In contrast, the fluorescence photons of the UHECR showers have wavelengths in the UV-pass region and therefore are only slightly affected by the efficiency of the filter (cf. fig. 6.3).

The difference between measurements taken with and without filter is the number of photons of interest. When taking measurements without the UV-pass filter the

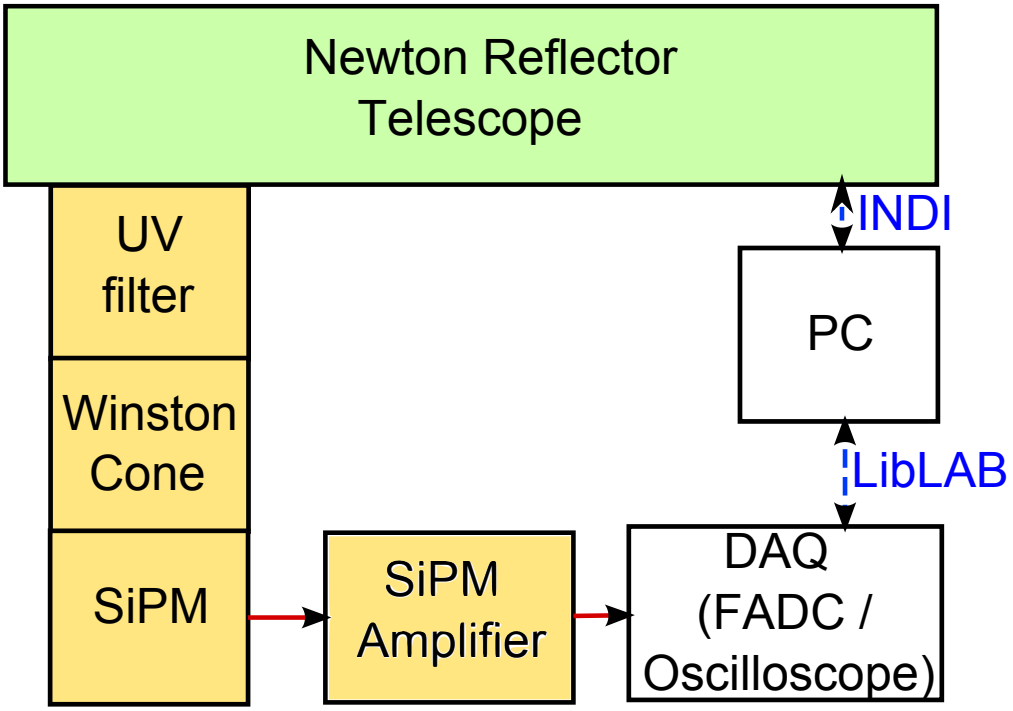

Figure 6.1: Experimental setup. The four yellow boxes (UV filter, Winston cone, SiPM, SiPM amplifier) symbolise the unit which is built into a box, cf. fig. 6.2, red box. The red lines describe the way of the signal and the blue lines stand for communication between the devices which works in both directions.

total number of night-sky brightness photons is of interest[1]. Therefore, the photon detection efficiency (PDE) of the SiPM has to be taken into account. As a consequence, the night-sky spectrum of Aachen has to be known. After unfolding the two functions the total number of photons can be calculated from the number of detected photons.

In contrast to measurements taken without filter, the *number of the detected photons* is of interest when taken data with filter. In this case, detected photons refers to the number of photons per pixel, i.e. the efficiencies of SiPM and Winston cone do not have to be considered since FAMOUS will use the identical layout. This reduction on the UV-pass range is possible since FAMOUS (cf. sec. 2.1.1) will use the same filter and therefore this is exactly the wavelength region of interest. This enables measurements without the knowledge of the night-sky spectrum of Aachen. If data was taken without filter it would be necessary to determine the number of photons in the UV-pass region.

The fluorescence telescopes at the Pierre Auger Observatory (cf. sec. 2.1.1) currently use UV-pass filters (M-UG 6) as well. The M-UG 6 is 3.25 mm thick whereas the new filter used for FAMOUS (UG 11) is only 1 mm thick. Additionally, the UG 11 has a higher and wider transmittance in the UV range and a lower and narrower transmittance in the red range which is proficient for the intentions (cf. fig. 6.3).

[1] within the wavelength band of the SiPM which acts as filter as well

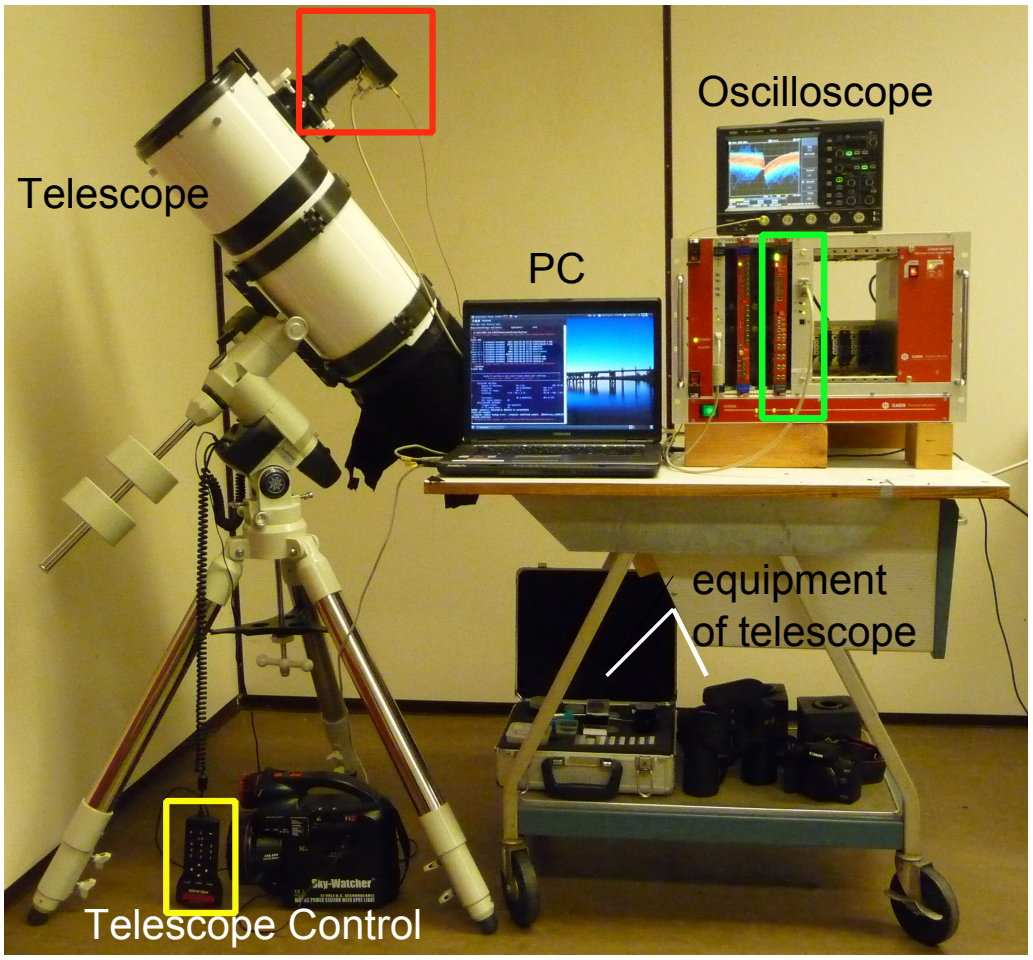

Figure 6.2: Photo of the experimental setup. The red box indicated the unit of UV-pass filter (if used), Winston cone, SiPM and SiPM amplifier. The green box mark the FADC and VM-USB units.

The UV-pass filter has to be built-in in front of the SiPM. As the SiPM is immediately behind the Winston cone, the filter is mounted in front of the Winston cone (cf. fig. 6.1).

6.2 Distinction of Stars and Background Light

The first issue of interest within the measurements is to demonstrate that the distinction of stars and background light is possible with the one-pixel-SiPM telescope. To demonstrate this two different kinds of measurements are performed. First, a sky scan of a region around a star is done with the oscilloscope. Second, the FADC was used to record traces of a star moving out of the field of view.

6.2.1 Sky Scan

Since the telescope has only one pixel it is not possible getting a picture of a star by just aligning it with the telescope and taking data. Instead, a certain region

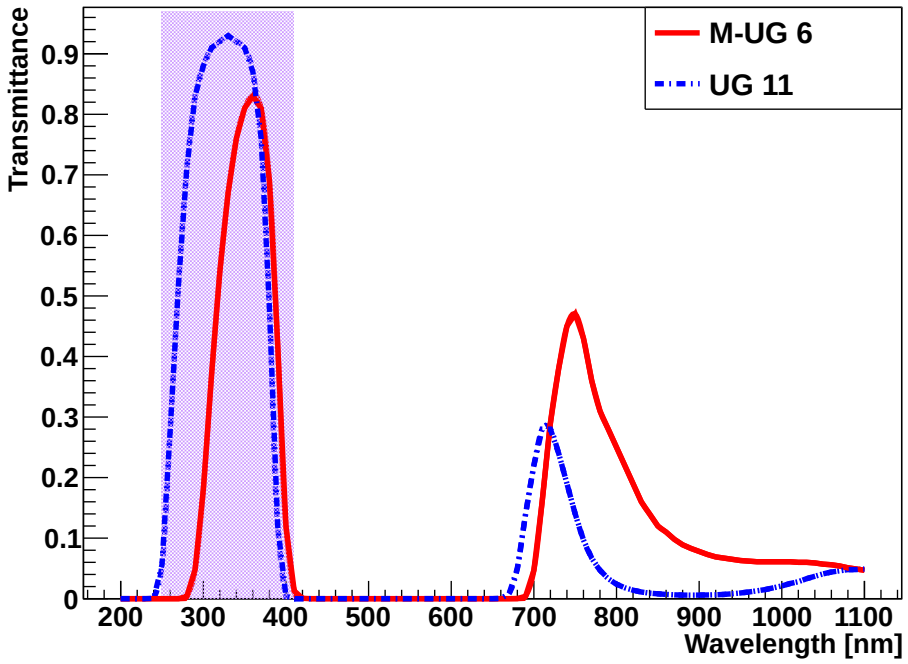

Figure 6.3: Comparison of the UV-pass filters used for FAMOUS (UG 11) and at the Pierre Auger Observatory (M-UG 6). The violet band symbolises the UV range. Data taken from [34] and [35].

of interest (wider than the field of view) has to be chosen which then is scanned with defined step sizes in right ascension and declination. This measuring method is called sky scan. As the field of view has a circular shape the sky region of interest can either be scanned with overlapping circles or blind spaces in between (cf. fig. 6.4). Therefore, a compromise has to be sought to find an adequate step size to neither have too large overlapping regions nor too large blind regions.

Within the performed sky scans for this thesis it was decided to minimize the blind regions by setting the step size of the right ascension to 0.5° and the step size of the declination to 0.55°. Regarding the field of view α_{fov} this results in an overlap in the direction of right ascension δ_{RA} of $\delta_{\text{RA}} = 0.21°$ and in declination δ_{DEC} of $\delta_{\text{DEC}} = 0.16°$. The blind region is reduced to a diagonal angular distance γ of $\gamma = 0.03°$ (cf. fig. 6.4).

To perform this measurement, a programme has been written for the oscilloscope. Since so far the analysis algorithm works only for the FADC, a random trigger is set at the oscilloscope and consequently the light flux is measured in arbitrary units. This does not raise any problem as the main interest of the sky scan is to demonstrate the ability of distinguishing stars from background light. For further purposes data was taken with the FADC.

The analysis programme allows to select a center of region of interest. A star is chosen to be this center enabling predictions about the stars position in the histogram

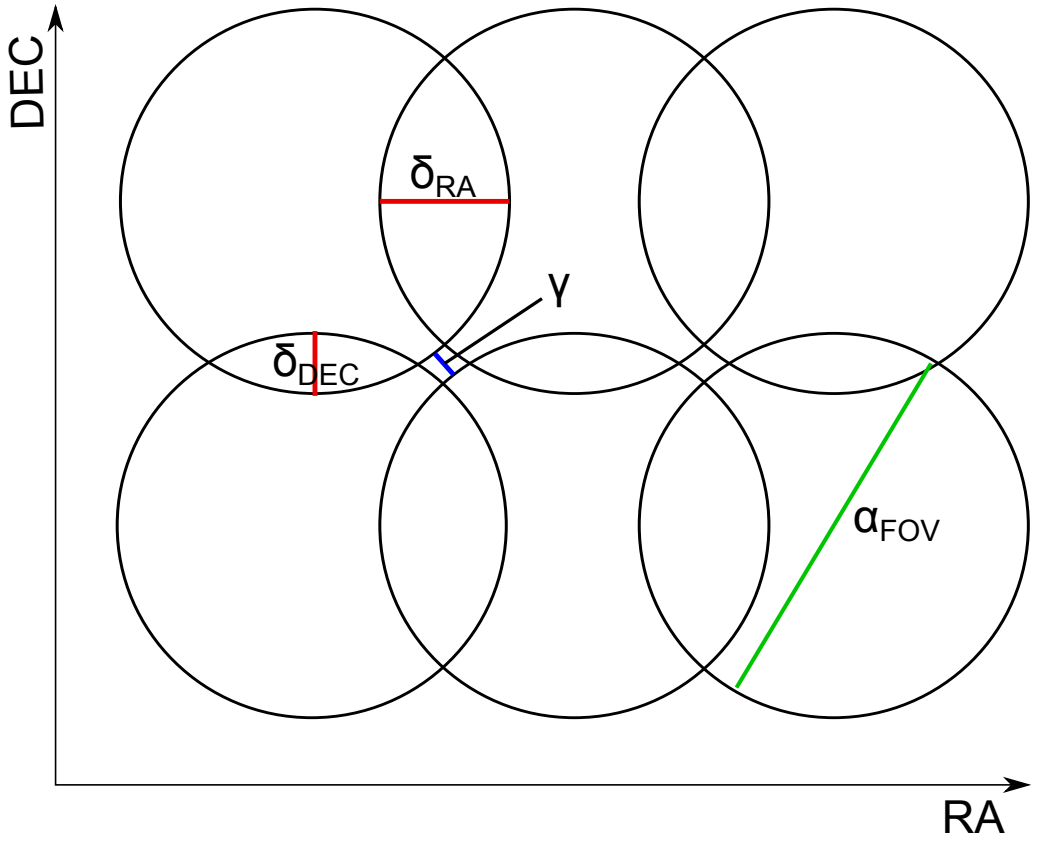

Figure 6.4: Schematics of a sky scan. The circles represent the field of view of the telescope. They overlap and a compromise has to be found to reduce blind spaces and not to have to large overlapping regions.

and to have a control if the resultant histogram corresponds to the expectations. Sky scans have been performed around to different, bright stars, one around Arcturus with an apparent magnitude of $V = -0.04$ mag and around Vega with an apparent magnitude of $V = 0.03$ mag (cf. fig. 6.5 and 6.6).

The first measuring point is at the smallest value of both declination and right ascension. In the following, first only the right ascension is increased step by step until its maximum. Having reached it, the telescope moves back to the minimal value of the right ascension and declination is increased by one step size. Due to this method, rising values in declination can also be interpreted as progress in time.

The sky scan around Arcturus was performed first. No UV-pass filter was used. Due to difficulties within the connection between the oscilloscope and the PC values of the light flux rate had to be written manually into the histogram. The first eight measuring points have to be regarded carefully since it had to be practiced how to take data manually. Furthermore, the conditions for measuring were difficult since the night was cloudy and the sky had to be observed carefully so that no clouds were in the region of interest. This method allows obviously only to identify visible clouds. Consequently, the measurement took about 1.5 hours. As it was already

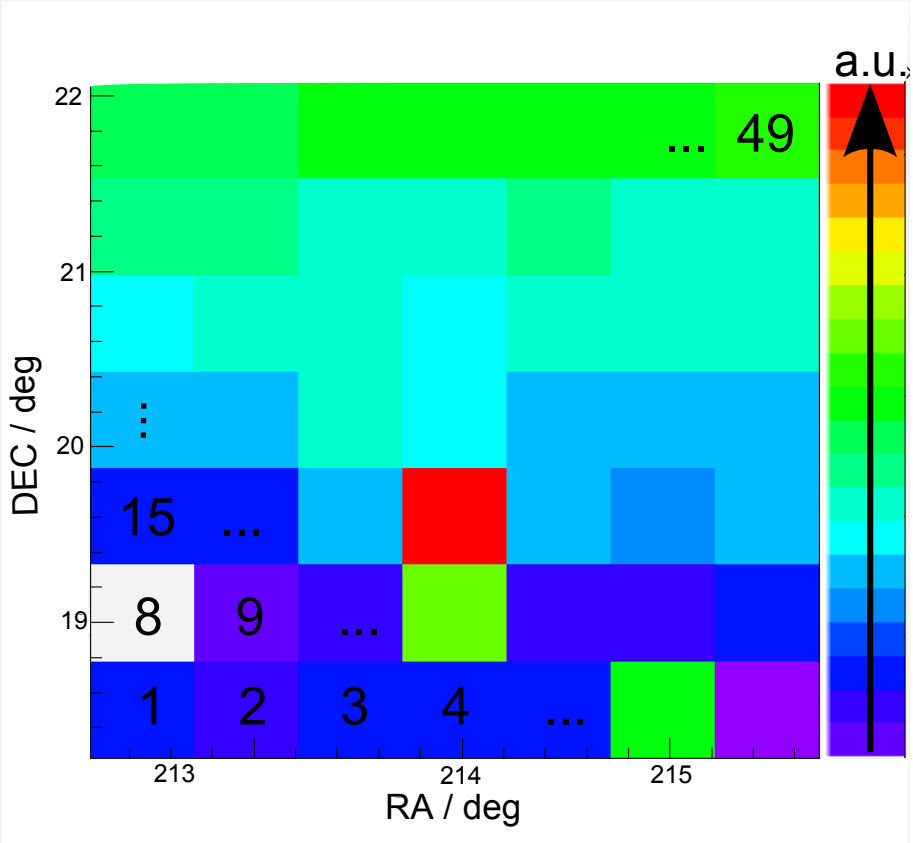

Figure 6.5: Sky scan around Arcturus without UV-pass filter. Measurements took about 1.5 hours. The star is clearly visible as red dot in the middle of the scan. The numbers symbolise the order of measurements. 49 data points were taken.

dawn, the sky got brighter which is visible in the sky scan. Anyway, the position of the star can clearly be determined.

As center of region of interest of the second sky scan Vega was chosen. The connection between oscilloscope and PC worked without problems. This time, the UV-pass filter was mounted. Here, too, the star is clearly visible in the histogram. The reason for having higher rates in two data points is the overlap of the field of views as explained before.

Consequently, it is possible to distinguish stars and background light with and without UV-pass filter.

6.2.2 Star Tracking

The second possibility to demonstrate the distinction between star and background light is to record FADC traces of a star and to compare it to data of a dark region. The time between the measurements should be short since the brightness of the night sky may vary during the night or even between different nights. Therefore, first traces of the starlight were recorded with the automatic star tracking of the telescope turned on. After a certain number of traces the star tracking was turned

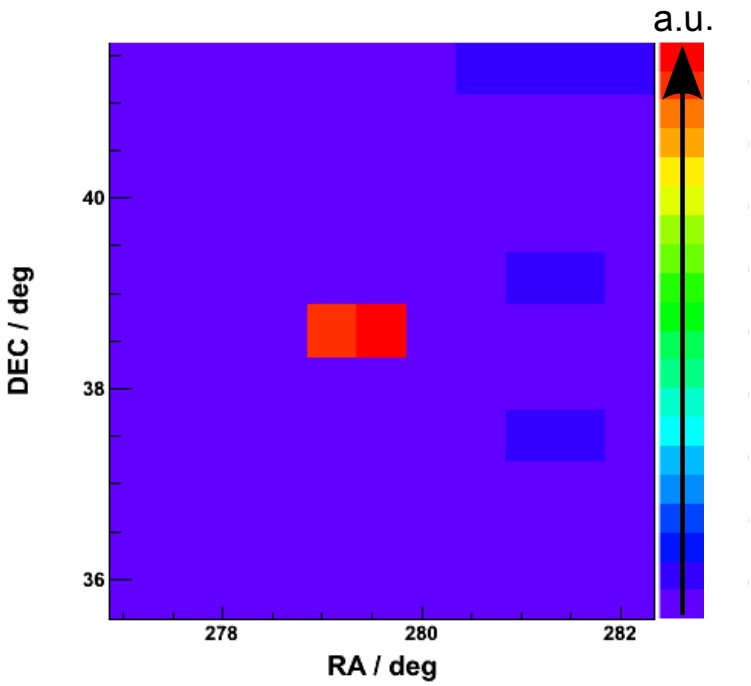

Figure 6.6: Sky scan around Vega with UV-pass filter. Vega is visible as red dot in the middle of the scan. 81 data points were taken.

off causing the star to move out of the field of view of the telescope. Since this takes only a small amount of time, the duration of the single measurements is selected to be short, i.e. 10 s. Two of these measurements were performed, the first started with taking data of Arcturus (3$^{\text{rd}}$ July, 2012 in Aachen) and the second with Vega (24$^{\text{th}}$ July, 2012 in Aachen). Both times the UV-pass filter was used. The results are shown in fig. 6.7 and 6.8. The background light of the measurement performed on the 3$^{\text{rd}}$ July, 2012, does not drop as deep as the second measurement, since the night was brighter (cf. fig. 6.9).

In both measurements star and background are clearly distinguishable. To verify that the steep decrease is due to the star moving out of the field of view (FOV), the time when the decrease is expected was calculated for the first sky measurement. For this, the relative velocity of the star in relation to Earth is needed. Stellarium [27] enables to determine the position of the star at a certain time. By calculating the differences in right ascension and declination over a predefined window of time, this velocity is determined:

$$v = \frac{\sqrt{\Delta_{\text{rec}}^2 + \Delta_{\text{dec}}^2}}{\Delta t} \tag{6.1}$$

with Δ_{rec} for the difference in right ascension and Δ_{dec} for the difference in declination. Like this, a velocity of $v = 0.00778° s^{-1}$ is calculated. Provided that the star has been focused exactly in the middle of the field of view the decrease is expected

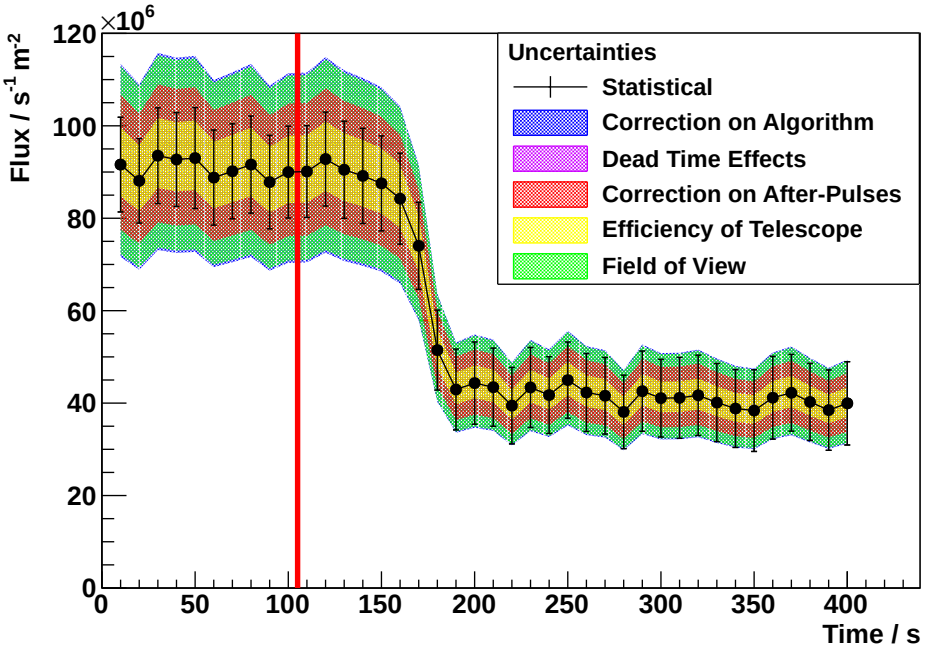

Figure 6.7: Star tracking Arcturus performed on 3rd July, 2012 in Aachen. The star tracking has been stopped at the time indicated by the red line, afterwards the star starts to move out of the field of view, causing a decrease in the rate. The units are characteristic for the telescope since the star is fully seen by the telescope.

after 44.2 s. An uncertainty of 5% on the FOV is estimated resulting in an expected decrease after $t_{\text{decrease}} = 44.2 \pm 2.2$ s. Comparing this time with the measured data shows a good agreement which verifies that the decrease is caused by the star leaving the FOV.

Consequently, the distinction of star and background light with FADC is possible as well.

6.3 Light Flux of the Night-Sky

The light flux of the night-sky is of great interest since the value is needed for simulations for the FAMOUS telescope. Data was taken during several nights at sites of different light pollution and during different lunar phases. Furthermore, the influence of the UV-pass filter was studied by taking data with and without the filter.

Different background luminosities

Data was taken during several nights. Within these nights the phase of the moon changed and the sky was visibly brighter during full moon. The issue of interest was to study whether differences are observable in the analysed traces recorded with UV-pass filter as well or not.

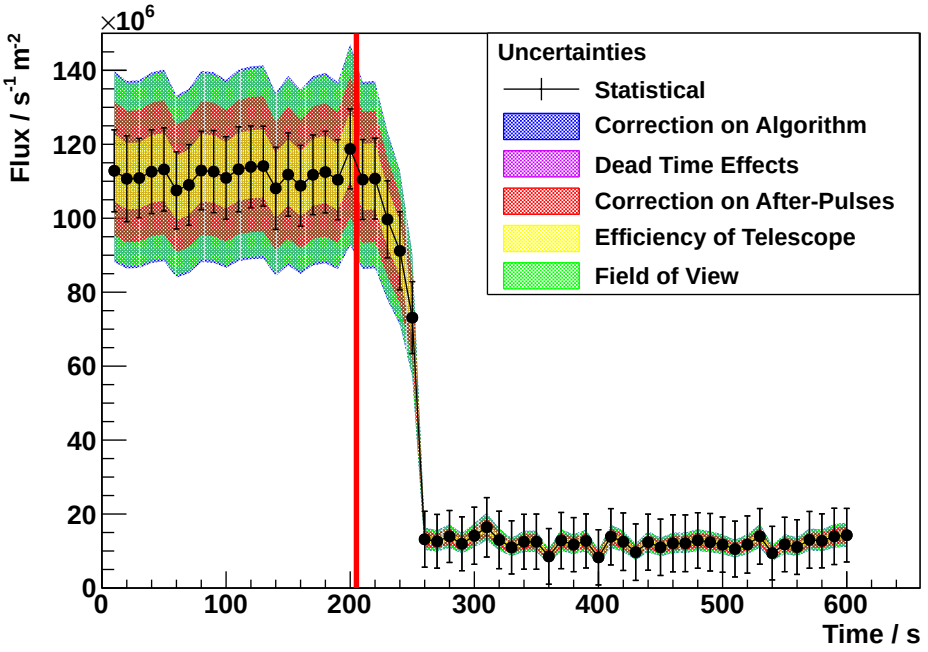

Figure 6.8: Star tracking Vega performed on 24$^{\text{th}}$ July, 2012 in Aachen. The star tracking has been stopped at the time indicated by the red line, afterwards the star starts to move out of the field of view, causing a decrease in the rate. The units are characteristic for the telescope since the star is fully seen by the telescope.

In figure 6.9 measurements of four different nights are shown. The first night (23$^{\text{rd}}$ June, 2012 in Aachen) the lunar phase was in between new moon and the first quarter. The second night (3$^{\text{rd}}$ July, 2012 in Aachen) was the brightest night of the year since the measurement was taken during the shortest night when the moon was full and this full moon was the lowest with the moon never setting behind the horizon [36]. During the third night (24$^{\text{th}}$ July, 2012 in Aachen) it was the first quarter of the moon phase and at the same observation site. The last measurement was taken only three days later but at a different observing site which is less effected by light pollution (27$^{\text{th}}$ July, 2012 in Eschauel, near Nideggen in the Eifel).

The statistical uncertainties of the measurements of the second night are higher since the measuring time was smaller and therefore the number of FADC traces which are used for the light flux calculation. The systematic uncertainties for higher rates are higher than for smaller rates since for data with low light fluxes the systematic uncertainties are diminished by subtracting the ones of dark count measurements. In case of high light fluxes the effects of the uncertainties of the FOV, the efficiency of the telescope and after-pulses have a greater absolute contribution and hence are not reduced much by the dark count systematic uncertainties which differ in the same direction. Some measurements show a slight increase in the light flux (especially the third one) which can be explained by the time of measuring. The sky already got slightly brighter since it was shortly before dawn (cf. fig. 6.10).

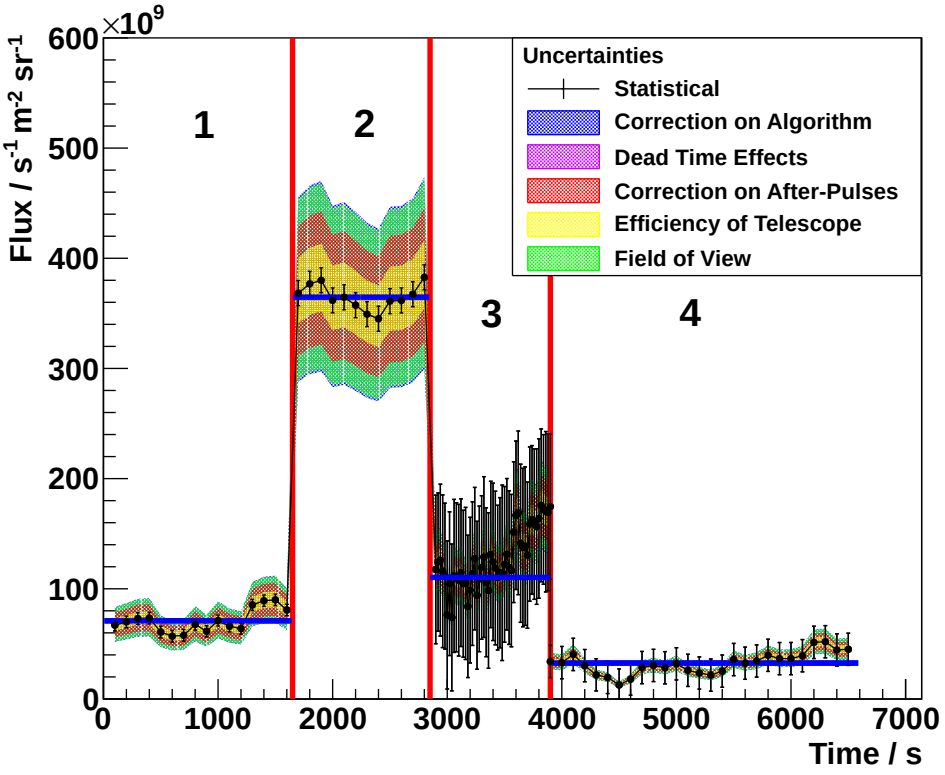

Figure 6.9: Background luminosity. The red lines represent the end of a measurement and therefore imply a time offset for the next measurement. The data was taken at 1) 23$^{\text{rd}}$ June, 2012 in Aachen; 2) 3$^{\text{rd}}$ July, 2012 in Aachen; 3) 24$^{\text{th}}$ July, 2012 in Aachen; 4) 27$^{\text{th}}$ July, 2012 in Eschauel, near Nideggen in the Eifel. The blue lines represent average values. For the third sector the last data points were not used for the calculation of the average since they increase steadily.

The background light flux rates are determined by fitting a constant to the data points with consideration of the statistical uncertainties. The results for the rates are shown in tab. 6.1. The statistical uncertainties of the rates are taken from the analysis with ROOT, the systematic uncertainties are determined from the graph. The fitted constants are in good agreement within the statistical uncertainties.

Consequently, the moon has a measurable effect also in the UV-pass range. Furthermore, the comparison between the third measurement taken in Aachen and the measurement in the Eifel have different results. This difference is due to light pollution. The measurements in Aachen are influenced a lot more by civilization caused light. An estimation can be calculated by subtracting the rate measured in the Eifel from the data taken three days earlier in Aachen. This results in a light pollution rate of $f_{\text{light pollution}}=(86.7 \pm 6.8\,^{+19.7}_{-15.3}) \cdot 10^9$ s^{-1}m^{-2}sr^{-1} (the first uncertainty is the statistical one, the second indicates the up- and downward systematic uncertainty, if not otherwise indicated this applies to all data).

Date	background light rate / 10^9 $s^{-1}m^{-2}sr^{-1}$
2012-06-23	$70.9 \pm 1.3\ ^{+18.9}_{-14.4}$
2012-07-03	$364.7 \pm 3.3\ ^{+84.7}_{-78.4}$
2012-07-24	$110.3 \pm 6.2\ ^{+26.1}_{-23.0}$
2012-07-27	$23.6 \pm 2.8\ ^{+6.4}_{-7.7}$

Table 6.1: Background light rates. The first uncertainty is the statistical one, the second indicates the up- and downward systematic uncertainty.

Light flux during dawn

At the end of the night in the Eifel (27th July, 2012), FADC traces were recorded during dawn. A steady steepening increase in the rate is observable as expected, cf. fig. 6.10.

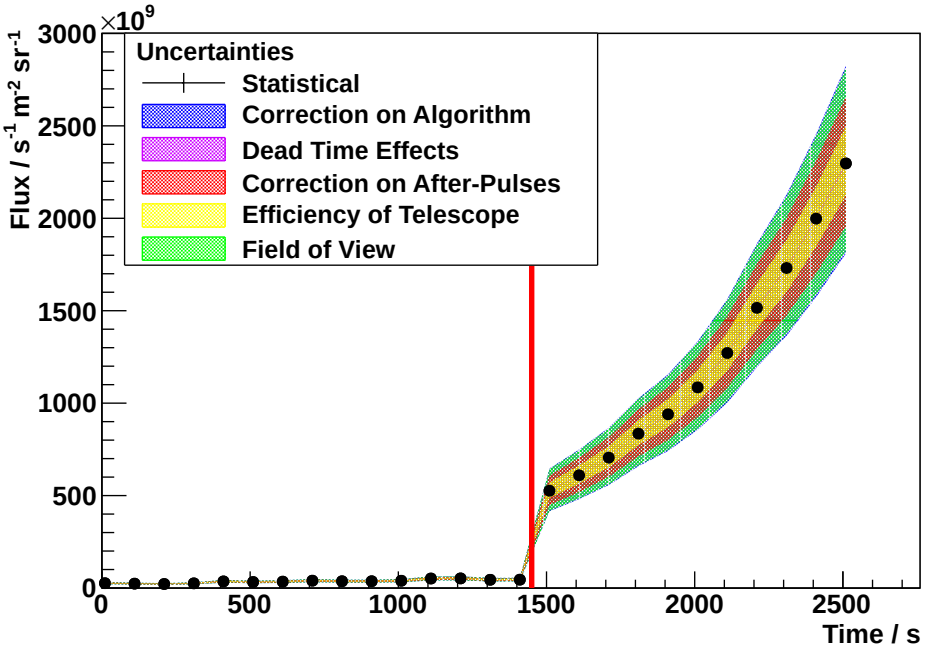

Figure 6.10: Dawn. The red line symbolises an interruption of the measurements of 1.5 hours. After the break, it was visibly brighter and some data point were taken during dawn.

Effects of the UV-pass filter

To demonstrate the effect of the UV-pass filter, data was taken with and without this filter during one night (23rd June, 2012 in Aachen). The measurement results are shown in fig. 6.11.

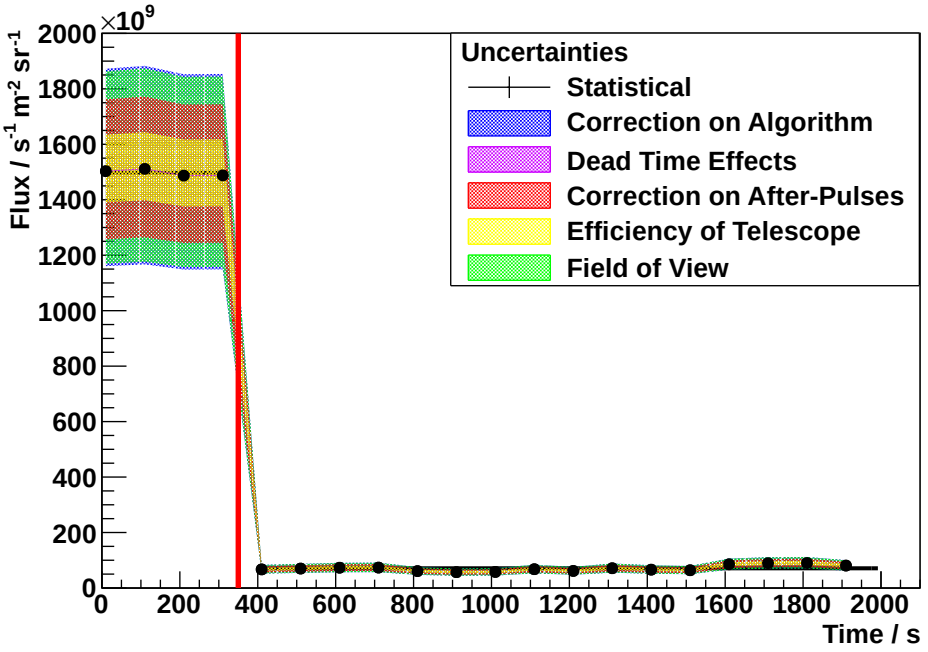

Figure 6.11: Effects of the UV-pass filter. The red line symbolises the change from measurements performed without filter (left) and with filter (right) and therefore an additional offset in time of 10 min. As expected the rate is higher in case of measuring without the filter. The black lines represent average values. The data was taken on 23$^{\text{rd}}$ June, 2012 in Aachen

As expected, the rate is higher in case of measuring without filter. The rate without filter is

$$f_{\text{without}} = (1497 \pm 3\,^{+343}_{-327}) \cdot 10^9\,\text{s}^{-1}\text{m}^{-2}\text{sr}^{-1}$$

and with filter

$$f_{\text{with}} = (70.9 \pm 1.3\,^{+10}_{-8}) \cdot 10^9\,\text{s}^{-1}\text{m}^{-2}\text{sr}^{-1} \quad .$$

This corresponds to a decrease to 4.7%.

6.4 Light Flux of Stars

Besides the determination of the light flux of the night-sky background, data was taken from two of the brightest stars of the night-sky, Arcturus and Vega. Care must be taken regarding the brightness of the stars since a UV-pass filter is used. Whereas Arcturus has a brighter apparent magnitude in total Vega is brighter in the UV-pass range of the filter: The brightness of Arcturus in the U-B-band is $UB_{\text{Arcturus}} = 1.27\,\text{mag}$ and of Vega $UB_{\text{Vega}} = -0.01\,\text{mag}$ [37]. Therefore, higher rates are expected for Vega.

Data was taken during two nights (3rd July, 2012 in Aachen and 24th July, 2012 in Aachen). The data is shown in fig. 6.12.

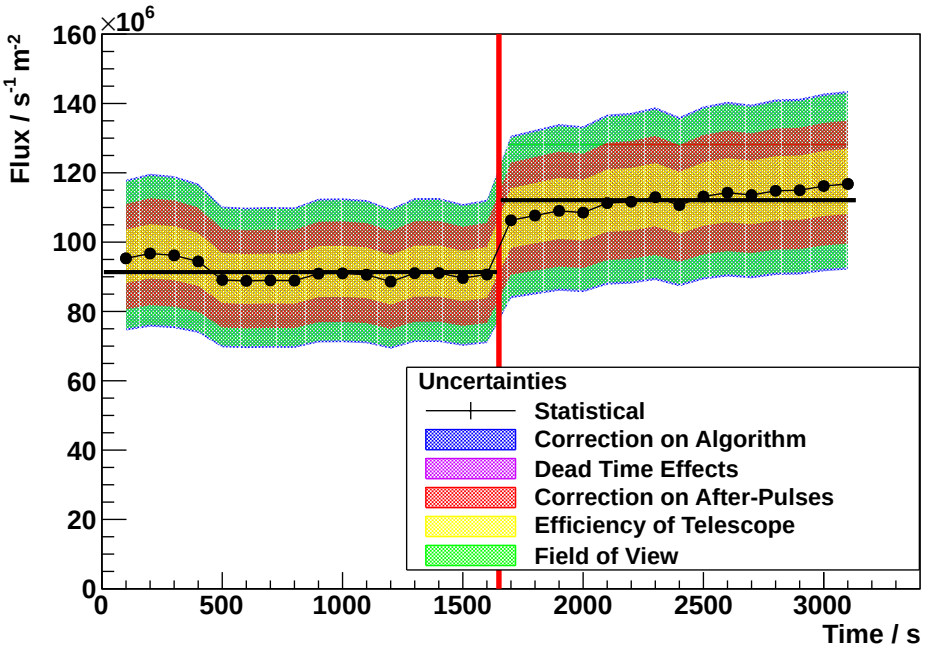

Figure 6.12: Comparison of the brightness of Arcturus (left, 3rd July, 2012 in Aachen) and Vega (right, 24th July, 2012 in Aachen). Data was taken with mounted UV-pass filter. Vega is brighter in the UV range. The black lines represent average values.

The results confirm the expectations. The light flux of Vega is with

$$f_{\text{Vega}} = (11.21 \pm 0.03\,^{+0.23}_{-0.25}) \cdot 10^7\,\text{s}^{-1}\text{m}^{-2}$$

higher than the light flux of Arcturus with

$$f_{\text{Arcturus}} = (9.13 \pm 0.03\,^{+0.22}_{-0.20}) \cdot 10^7\,\text{s}^{-1}\text{m}^{-2} \quad .$$

The fitted constants are in good agreement within the statistical uncertainties. The values are in reference to the telescope and not to steradian since the star was fully visible for the SiPM.

6.4.1 Calibration of the Telescope

The measurement of Vega and calculating the light flux of the star enables a calibration of the telescope. Further on a rough estimation is described without uncertainty calculation since the issue of interest is whether the scale of measurement results fits with the expectation. The light flux of Vega with U-filter (i.e. ultraviolet light passes the filter) has been determined in [38] to $f_{\text{Vega,U}} = 4.22 \cdot 10^{-11}\,\text{Js}^{-2}\text{m}^{-2}\text{nm}^{-1}$. The

U-filter used has maximal transmission at a wavelength of $\bar{\lambda} = 373.5\,\text{nm}$ and a full width at half maximum (FWHM) of FWHM $= 48.5\,\text{nm}$. By comparison, the UG 11 UV filter used within this thesis has a maximal transmission of $\bar{\lambda}_{\text{UG 11}} \approx 360\,\text{nm}$ and FWHM $\approx 100\,\text{nm}$. Assuming the light flux is constant within the bandwidth and the transmittance of the filter is Gaussian distributed, the integrated flux I can be calculated with

$$I = \int_{-\infty}^{\infty} f_{\text{Vega,U}} \cdot \exp\left(-\frac{1}{2}\left(\frac{\lambda - \bar{\lambda}}{\sigma}\right)^2\right) d\lambda = \sqrt{2\pi}\sigma f_{\text{Vega,U}} \tag{6.2}$$

with σ being the standard deviation. The relation between σ and FWHM is given by

$$\sigma = \frac{\text{FWHM}}{2.4584} \tag{6.3}$$

leading to an integrated flux of $I = 2.18 \cdot 10^{-9}\,\text{J}\,\text{s}^{-1}\text{m}^{-2} = 1.36 \cdot 10^{10}\,\text{eV}\,\text{s}^{-1}\text{m}^{-2}$.

A photon at $\bar{\lambda}$ has the energy E

$$E = c\bar{\lambda}^{-1}h \simeq 3.32\,\text{eV} \tag{6.4}$$

with c as the velocity of light and h the Planck constant. This results in an integrated photon flux $f_{\text{Vega,int}}$ of

$$f_{\text{Vega,int}} = \frac{I}{E} = 4.10 \cdot 10^9\,\frac{\text{photons}}{\text{s}\,\text{m}^2} \quad . \tag{6.5}$$

Finally, the integrated photon flux is multiplied by the entrance surface size $A_{\text{objective}}$ and the efficiencies of the telescope $\epsilon_{\text{telescope}} = 0.7$, the UV-pass filter $\epsilon_{\text{filter}} = 0.84$, the Winston cone $\epsilon_{\text{Winston}} = 1$ and the SiPM due to the photon detection efficiency (PDE) $\epsilon_{\text{SiPM}} = 0.30$ are taken into account resulting in a rate expected to be detected by the telescope of

$$f_{\text{Vega,telescope,1}} = f_{\text{Vega,int}} \cdot \epsilon_{\text{telescope}} \cdot \epsilon_{\text{filter}} \cdot \epsilon_{\text{Winston}} \cdot \epsilon_{\text{SiPM}} = 24\,\text{MHz} \quad . \tag{6.6}$$

The values for the efficiencies are only approximated values providing that the efficiencies are constant. This is obviously only a rough estimation resulting in a too large expected light flux. Additionally, the light flux is not constant over the bandwidth of the U-filter which increases the effect.

Another approach has been performed by M. Stephan, starting with the approximation that the star emits black-body radiation [32]. The spectrum of the radiation is adapted to the spectrum of Vega measured in [38]. In contrast to the previous

approach, the efficiency of the UV-pass filter is not implemented as constant value but the curve plotted in fig. 6.3 is implemented. Additionally, an atmospheric filter is used since photons are absorbed and scattered on fine particles known as aerosol. This approach leads to a light flux of $f_{\text{Vega,telescope,2}} \approx 10.0\,\text{MHz}$.

To compare these two values to the measured one, the result of the light flux of Vega has to be converted from SI-units into a characteristic value for the telescope. This can be achieved by multiplying by the aperture entrance size $A_{\text{objective}}$ (cf. eq. (5.19)). This results in a detected light flux of Vega with the telescope of 3.6 MHz. The approaches predict too high light flux rates. This can be explained by the approximations made within the approaches. Neither the light flux of Vega nor the efficiencies have constant values and for the approaches maxima were used. Additionally, the atmosphere between Vega and the telescope has a non negligible effect. But the angle at which Vega appears on the night-sky is not taken into consideration, the approach assumes vertical entrance of the light. This means less atmosphere between star and telescope and therefore higher rates. Furthermore, the atmosphere itself can only be estimated since it depends on many factors like temperature, humidity and the density of aerosol. Consequently, this may explain the high differences. The measured flux is in the same magnitude as expected.

7. Conclusion and Outlook

Light detection with silicon photomultipliers (SiPMs) is a new promising technology. For demonstrating that the detection of ultra-high-energy cosmic ray (UHECR) showers is possible with this technology, the FAMOUS telescope is being developed and a programme for its simulation is currently being written.

For the simulation, background light fluxes are essential to implement a trigger to start measurements when UHECR showers arrive.

Within this thesis, these background light measurements were performed. The background is the night-sky brightness (NSB) consisting of natural light and air pollution. Measurements have been performed both with and without a UV-pass filter revealing that the light contribution in the UV range is small compared to the light in the whole wavelength range. Background luminosity data was taken during several nights at different lunar phases and observation sites showing differences in the light flux. All measured fluxes are within the range of $(23 - 365) \cdot 10^9\,\mathrm{s^{-1}m^{-2}sr^{-1}}$.

Another issue of interest studied was the distinction of stars and the background light with the one-pixel-SiPM-telescope. Data was taken both with an oscilloscope and an FADC. It could be demonstrated that the stars cause higher light fluxes both in the whole wavelengths spectrum and the UV range only and therefore the distinction was successful.

Furthermore, differences in the light fluxes of different stars are detectable. Expectations about the brightness difference of Arcturus and Vega are confirmed.

The measurements of the brightness of Vega enabled a calibration of the telescope revealing that the measured flux is of the same magnitude as expected.

In the context of the FAMOUS project the next steps are to implement the NSB values into the simulation and to run it to find the optimal parameters for the telescope. Additionally, a prototype is constructed to enable first light detection with a silicon photomultiplier telescope within this year.

References

[1] J. Bluemer, R. Engel, and J. Hoerandel, *Cosmic Rays from the Knee to the Highest Energies*, Prog.Part.Nucl.Phys., 63 (2009), pp. 293–338.

[2] Pierre Auger Observatory, *¿Por qué el sur de Mendoza?* `http://visitantes.auger.org.ar/index.php/el-observatorio/por-que-malargue.html`. visited 23.08.2012.

[3] Pierre Auger Observatory, *Skizze des Auger Arrays*. `http://www.auger.de/public/sd.de.html`. visited 27.08.2012.

[4] I. Allekotte *et al.*, *The Surface Detector System of the Pierre Auger Observatory*, Nucl.Instrum.Meth., A586 (2008), pp. 409–420.

[5] C. Meurer and N. Scharf, *HEAT - a low energy enhancement of the Pierre Auger Observatory*, Astrophys.Space Sci.Trans., 7 (2011), pp. 183–186.

[6] J. Abraham *et al.*, *The Fluorescence Detector of the Pierre Auger Observatory*, Nucl.Instrum.Meth., A620 (2010), pp. 227–251.

[7] M. Lauscher *et al.*, *FAMOUS: A prototype silicon-photomultiplier telescope for the fluorescence detection of ultra-high-energy cosmic rays*, SPIE, 8460 8460-56 (2012).

[8] T. Niggemann, *New Telescope Design with Silicon Photomultipliers for Fluorescence Light Detection of Extensive Air Showers*, master's thesis, RWTH Aachen University, 2012.

[9] M. Stephan *et al.*, *Future use of silicon photomultipliers for the fluorescence detection of ultra-high-energy cosmic rays*, SPIE, 8155 81551B-1 (2011).

[10] A. Weigert, H. Wendker, and L. Wisotzki, *Astronomie und Astrophysik*, Wiley-VCH Verlag GmbH & Co. KGaA, 2009.

[11] R. E. Zissell, *The S(10) System Applied to Celestial, Non-Point-Source Objects in Determining Surface Brightness*, The Journal of the American Association of Variable Star Observers, 29 (2001), pp. 129 – 131.

[12] Benn, Chris R. and Ellison, Sara L., *La palma night-sky brightness*. `http://www.ing.iac.es/Astronomy/observing/conditions/skybr/skybr.html`. Isaac Newton Group of Telescopes; visited 23.08.2012.

[13] Benn, Chris R. and Ellison, Sara L., *La palma night-sky brightness*, (1999).

[14] K. Krisciunas and B. E. Schaefer, *A model of the Brightness of Moonlight*, Astronomical Society of the Pacific, Publications, 103 (1991), pp. 1033–1039.

[15] D. Renker and E. Lorenz, *Advances in solid state photon detectors*, Journal of Instrumentation, 4 (2009). P04004.

[16] J. Rennefeld, *Studien zur Eignung von Silizium Photomultipliern für den Einsatz im erweiterten CMS Detektor am SLHC*, Diplomarbeit, RWTH Aachen University, 2010.

[17] Hammamatsu, *Photomultiplier Tube and Related Product.* `http://jp.hamamatsu.com/products/sensor-etd/pd002/index_en.html`. visited 11.09.2012.

[18] B. Dolgoshein *et al.*, *Large area UV SiPMs with extremely low cross-talk*, Nuclear Instruments & Methods In Physics Research Section A, (2011).

[19] M. Lauscher, *Characterisation Studies of Silicon Photomultipliers for the Detection of Fluorescence Light from Extensice Air Showers*, master's thesis, RWTH Aachen University, 2012.

[20] CAEN, *V1729 data sheet.* `http://www.caen.it/csite/CaenProd.jsp?parent=11&idmod=465`. visited 24.08.2012.

[21] Wiener Plein & Baus GmbH, *VM-USB VME controller.* `http://www.wiener-d.com/products/18/70.html`. visited 24.08.2012.

[22] D. Terhorst *et al.*, *LibLAB library.* `http://liblab.physik.rwth-aachen.de/`. visited 21.08.2012.

[23] LeCroy, *WaveJet 354A.* `http://www.lecroy.com/oscilloscope/oscilloscopemodel.aspx?modelid=2000`. visited 24.08.2012.

[24] R. Winston, J. Miñano, W. Welford, and P. Benítez, *Nonimaging optics*, Academic Press, 2005.

[25] S. Mann, *Measurement of the UV Reflectivity of Aluminium in Different Stages of Oxidation.* bachelor's thesis, RWTH Aachen University, 2012.

[26] Hamamatsu, *Silicon Photomultiplier S10362-33-100C.* `http://sales.hamamatsu.com/en/products/solid-state-division/si-photodiode-series/mppc/part-s10362-33-100c.php`. visited 23.08.2012.

[27] *Stellarium.* `http://www.stellarium.org/`. visited 23.08.2012.

[28] *INDI Concepts.* `http://indilib.org/index.php?title=INDI_Concepts`. visited 23.08.2012.

[29] *ROOT website.* `http://root.cern.ch/drupal/`. visited 28.08.2012.

[30] P. Eckert *et al.*, *Characterisation studies of silicon photomultipliers*, Nuclear Instruments and Methods in Physics Research Section A, Volume 620, Issue 2-3, p. 217-226., (2010).

[31] T. Hebbeker, *Statistik - Fehlerrechnung - Auswertung von Messungen*. Januar 2012.

[32] M. Stephan, *private communication*, 2012.

[33] P. Hallen, *Determination of the recovery time of silicon photomultipliers*. bachelor's thesis, 2011.

[34] SCHOTT, *Schott Website*. `http://www.schott.com/german/index.html`. visited 04.09.2012.

[35] SCHOTT, *UG11 data sheet*. `http://www.schott.com/advanced_optics/german/download/schott_uv_bandpass_ug11_2008_e.pdf`. visited 04.09.2012.

[36] Planetarium Hamburg, *Der Sternenhimmel im Juli 2012*. `http://www.planetarium-hamburg.de/print/sterne/monat/`. visited 07.07.2012.

[37] Centre de Données astronomiques de Strasbourg, *Bright Star Catalogue, 5th Revised Ed.* `http://vizier.u-strasbg.fr/viz-bin/VizieR-5?-out.add=.&-source=V/50/catalog&HR=7001`, `http://vizier.u-strasbg.fr/viz-bin/VizieR-5?-out.add=.&-source=V/50/catalog&HR=5340`. visited 07.09.2012.

[38] L. Colina, R. Bohlin, and F. Castelli, *Absolute Flux Calibrated Spectrum of Vega*, Instrument Science Report CAL/SCS-008, (1996).

Acknowledgements

An dieser Stelle möchte ich mich bei allen bedanken, die mir diese Arbeit ermöglicht haben und mich dabei unterstützt haben.

Ein großer Dank gilt Herrn Prof. Dr. Hebbeker für die Möglichkeit, in diesem interessanten Arbeitsgebiet meine Arbeit zu schreiben und somit einen Einblick von dem Arbeiten in einer internationalen Kollaboration zu erhalten.

Insbesondere bedanke ich mich bei meinem Betreuer Maurice Stephan und der gesamten Auger Arbeitsgruppe für die große Unterstützung, viele hilfreiche Diskussionen und das freundliche Arbeitsklima.

Außerdem bedanke ich mich herzlich bei meinen beiden Bürokollegen und Freunden Oskar Hofmann und Ania Koob für die fröhliche Atmosphäre in unserem Büro.

Des weiteren möchte ich noch Markus Lauscher, Tim Niggemann, Maurice Stephan und Sebastian Thüer für das Korrekturlesen meiner Arbeit danken.

Zu guter Letzt danke ich meiner Familie und meinen Freunden für ihre Geduld und die Unterstützung, wann immer sie nötig war.

Erklärung

Hiermit versichere ich, dass ich diese Arbeit einschließlich beigefügter Zeichnungen, Darstellungen und Tabellen selbstständig angefertigt und keine anderen als die angegebenen Hilfsmittel und Quellen verwendet habe. Alle Stellen, die dem Wortlaut oder dem Sinn nach anderen Werken entnommen sind, habe ich in jedem einzelnen Fall unter genauer Angabe der Quelle deutlich als Entlehnung kenntlich gemacht.

Aachen, den 15. September 2012

Rebecca Meißner